iScience

Article

# Resistance to spindle inhibitors in glioblastoma depends on STAT3 and therapy induced senescence

## Graphical abstract

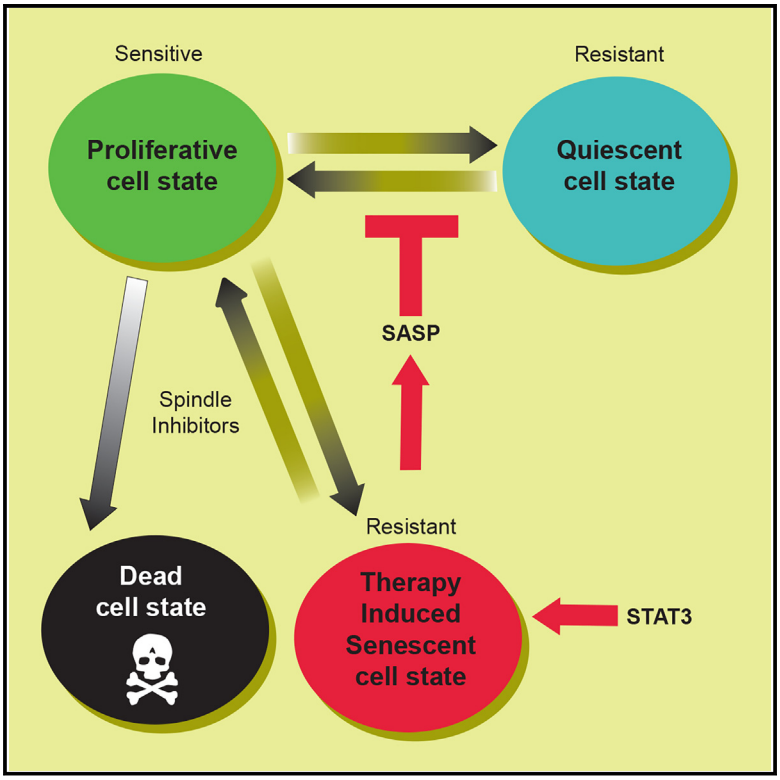


## Highlights

- Resistance to spindle inhibitors limits their efficacy in glioblastoma and depends on STAT3
- Resistance goes hand in hand with development of therapy induced senescence (TIS)
- Resistant GBMs consist of proliferative, quiescent, and TIS subpopulations
- TIS cells secrete TGFβ, which induces quiescence and resistance in proliferative cells

## Authors

Natanael Zarco, Athanassios Dovas, Virginea de Araujo Farias, ..., Peter Canoll, Steven S. Rosenfeld, Rajappa S. Kenchappa

## Correspondence

rosenfeld.steven@mayo.edu

## In brief

Molecular biology; Cell biology; Cancer

Zarco et al., 2024, iScience 27, 111311
December 20, 2024 
https://doi.org/10.1016/j.isci.2024.111311

CellPress

iScience

CellPress
OPEN ACCESS

Article

# Resistance to spindle inhibitors in glioblastoma depends on STAT3 and therapy induced senescence

Natanael Zarco,[1] Athanassios Dovas,[2] Virginea de Araujo Farias,[3,7] Naveen K.H. Nagaiah,[3] Ashley Haddock,[1] Peter A. Sims,[4] Dolores Hambardzumyan,[5] Christian T. Meyer,[6] Peter Canoll,[2] Steven S. Rosenfeld,[1,3,8,*] and Rajappa S. Kenchappa[1,3]

[1]Department of Cancer Biology, Mayo Clinic, Jacksonville, FL 32224, USA
[2]Department of Pathology and Cell Biology, Columbia University Irving Medical Center, New York, NY 10032, USA
[3]Department of Neurosurgery, Mayo Clinic, Jacksonville, FL 32224, USA
[4]Department of Systems Biology, Columbia University Irving Medical Center, New York, NY 10032, USA
[5]Departments of Oncological Sciences and Neurosurgery, Mount Sinai School of Medicine, New York, NY 10029, USA
[6]Duet Biosystems, Nashville, TN 37212, USA
[7]Present address: Department of Neurosurgery, University of Alabama at Birmingham, Birmingham, AL, USA
[8]Lead contact
*Correspondence: rosenfeld.steven@mayo.edu
https://doi.org/10.1016/j.isci.2024.111311

## SUMMARY

While mitotic spindle inhibitors specifically kill proliferating tumor cells without the toxicities of microtubule poisons, resistance has limited their clinical utility. Treating glioblastomas with the spindle inhibitors ispinesib, alisertib, or volasertib creates a subpopulation of therapy induced senescent cells that resist these drugs by relying upon the anti-apoptotic and metabolic effects of activated STAT3. Furthermore, these senescent cells expand the repertoire of cells resistant to these drugs by secreting an array of factors, including TGFβ, which induce proliferating cells to exit mitosis and become quiescent—a state that also resists spindle inhibitors. Targeting STAT3 restores sensitivity to each of these drugs by depleting the senescent subpopulation and inducing quiescent cells to enter the mitotic cycle. These results support a therapeutic strategy of targeting STAT3-dependent therapy-induced senescence to enhance the efficacy of spindle inhibitors for the treatment of glioblastoma.

## INTRODUCTION

The prognosis for glioblastoma (GBM) remains dismal, so there is a desperate need to develop more effective therapies.[1] An example is illustrated by a group of anti-proliferative drugs that target the mitotic spindle without affecting microtubules,[2–4] which in this report we refer to as *spindle inhibitors*. These drugs are devoid of the neurotoxicity of microtubule poisons, and include ispinesib, alisertib, and volasertib, which inhibit Kif11, aurora kinase A, and Polo-like kinase, respectively. Although these drugs are CNS penetrant[5–7] and are active against a variety of tumor cells, including GBM stem cells,[3,7,8] the emergence of treatment resistance has limited their efficacy. We had determined that in the case of the Kif11 inhibitor ispinesib, resistance in GBM depends on two functions of STAT3.[9] The first requires SRC phosphorylation at Y705, which induces STAT3 to stimulate transcription of pro-survival genes. The second requires EGFR pathway-mediated phosphorylation at S727, sending STAT3 to the mitochondria where it activates complexes I and II of the electron transport chain (ETC) and inhibits cytochrome *c* release in the penultimate stage of apoptosis.[9–12] This explains why combined inhibition of both of SRC and EGFR is required to restore ispinesib sensitivity. The efficacy of ispinesib in orthotopic GBM models can be significantly enhanced by co-administering saracatinib, an CNS penetrant combined SRC/EGFR inhibitor. We also found that ispinesib resistance goes hand in hand with the downregulation of mitotic and spindle checkpoint pathways; upregulation of TGFβ, EMT, and STAT3 pathways; a proneural-to-mesenchymal transcriptional shift; resistance to apoptosis; and both cellular and nuclear enlargement.[9]

This work raises further questions that are the focus of our current study. Like ispinesib, both alisertib and volasertib arrest cells in $G_2M$, so we wish to know if resistance to these drugs also depends on STAT3. In addition, the cellular enlargement and nuclear atypia that we see in ispinesib resistance are reminiscent of the process of senescence. Although first described as a form of *irreversible* mitotic exit that occurs during aging,[13] senescence can also develop in malignant cells in response to therapy,[14,15] where it is referred to as therapy induced senescence (TIS). TIS tumor cells secrete an array of factors, referred to as the *senescence associated secretory phenotype (SASP)*, which supports tumor growth, stemness, and angiogenesis; and which suppresses anti-tumor immunity.[16–20] In addition, one of these SASP factors, TGFβ, induces GBM cells to enter quiescence, a state where cells *reversibly* exit the mitotic cycle.[21] Since spindle inhibitors are only cytotoxic during the cell cycle, quiescent cells are therefore intrinsically resistant to these drugs. These findings imply that resistance to spindle inhibitors

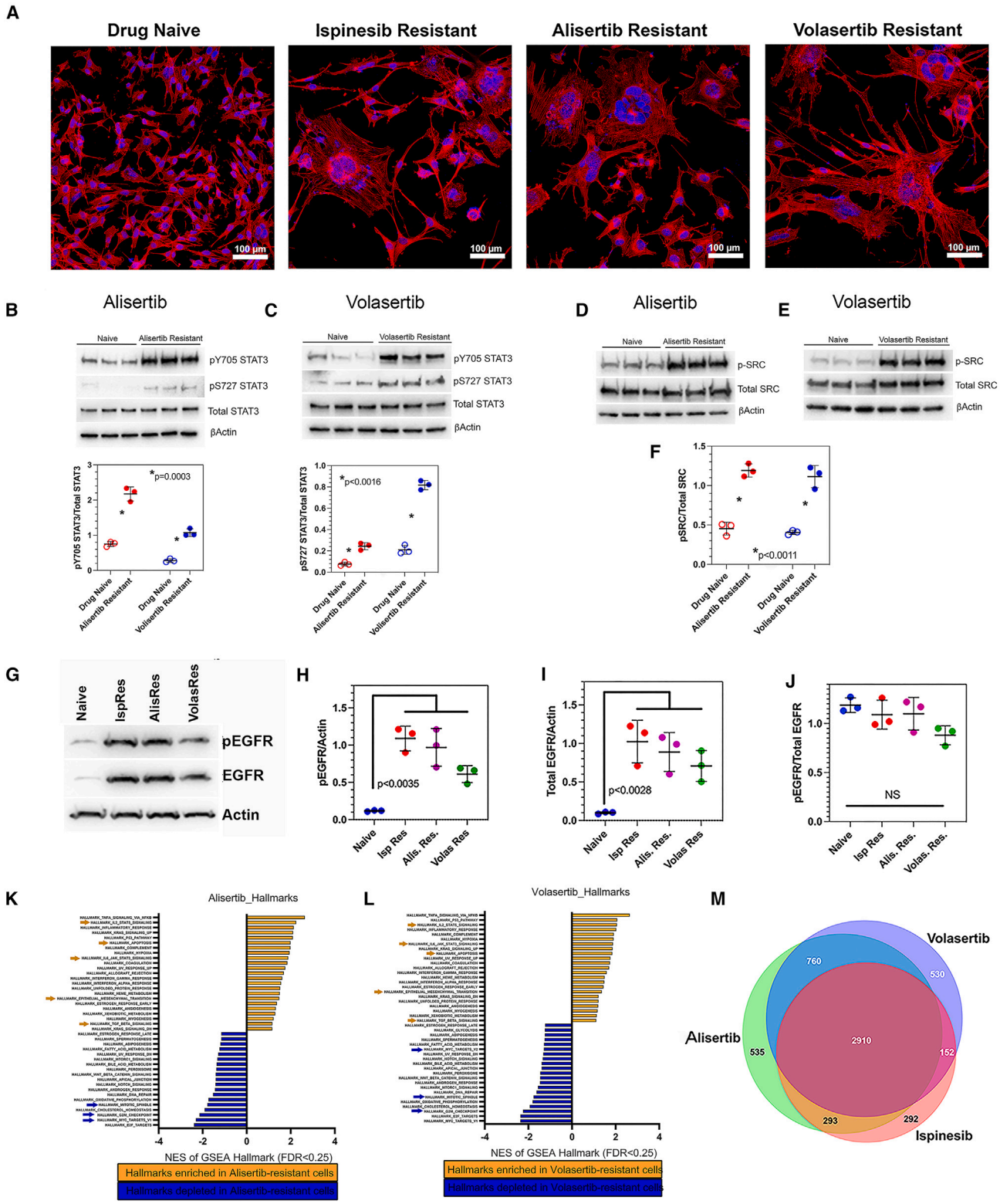


*(legend on next page)*

reflects a dynamic interplay between TIS, proliferative, and quiescent subpopulations. We propose that TIS cells resist these drugs by activating STAT3, which suppresses the apoptosis that ordinarily follows prolonged $G_2M$ arrest. We also propose that through their SASP, TIS cells suppress mitosis in many of the non-TIS cells, further expanding the populations of cells that can resist spindle inhibitors. In this report, we determine that resistance to all three spindle inhibitors relies on both STAT3 and TIS, and have developed a model that may guide future translational applications of these findings.

## RESULTS

### GBM cells resistant to ispinesib, alisertib, and volasertib share a common phenotype

We generated alisertib and volasertib resistant murine *Trp53/Pten*-co-deleted GBM cell lines (*referred to as Trp53/Pten(−/−)*) by exposing naive cells to drug for three weeks. As in the case of ispinesib, resistance to these other two spindle inhibitors is accompanied by marked cellular and nuclear enlargement and multinucleation in a substantial fraction (Figure 1A), along with increases in pY705 STAT3, pS727 STAT3 (Figures 1B and 1C), activated SRC, and activated and total EGFR (Figures 1D–1J). Note that in the case of EGFR, the increase in activated receptor reflects a corresponding increase in total receptor content (Figure 1J). Bulk RNAseq of alisertib and volasertib resistant cells reveal patterns of pathway activation very similar to those for ispinesib resistance.[9] These include down-regulation of the mitotic spindle, $G_2M$ checkpoint, and c-MYC related pathways (*blue arrows in* Figures 1K and 1L) and up-regulation of STAT3, STAT5, TGFβ, apoptosis, and epithelial-mesenchymal transition (EMT) related pathways (*gold arrows in* Figures 1K and 1L). Nearly 3000 (53%) of these upregulated genes are shared among spindle inhibitor resistant cells (Figure 1M), consistent with a shared resistance mechanism.

### Resistant GBM cells share therapeutic vulnerabilities in common, reflecting a shared STAT3-dependent mechanism

We had previously shown that saracatinib, a dual EGFR/SRC inhibitor that blocks Y705 and S727 phosphorylation of STAT3, reverses Ispinesib resistance.[9] We now show that ispinesib resistance automatically confers resistance to alisertib and volasertib as well (Figure 2A), implying that resistance to these latter drugs is also STAT3 dependent and consistent with the upregulation of pY705 STAT3 and pS727 STAT3 that alisertib and volasertib resistance induces (Figures 1B and 1C, *above*). This explains why saracatinib, a combined EGFR and SRC inhibitor that we previously showed blocks dual phosphorylation of STAT3[9] also reverses alisertib and volasertib resistance (Figure 2B). SH5-07, an allosteric inhibitor of STAT3[22] that reverses ispinesib resistance[9] likewise reverses alisertib and volasertib resistance (Figure 2C) in both murine and human (612, L1) GBM lines. Like the murine GBM lines, both of these human lines also upregulate pY705 and pS727 STAT3 upon becoming ispinesib resistant (Figure S1). We also examined if adding saracatinib to alisertib or volasertib improves survival over either drug alone in a *Trp53*-deleted (*Trp53(−/−)*) genetically engineered mouse model (GEMM), as it does with ispinesib.[9] While alisertib (Figure 2D, *left*) alone prolongs median survival over vehicle (*33* versus *45.5 days; $p < 0.0001$ log-rank test*), combining it with saracatinib is significantly more effective than alisertib alone (*45.5* versus *53.5 days, p=0.0001, log-rank test*). Likewise, combining volasertib (Figure 2D, *right*) with saracatinib significantly prolongs median survival over either drug alone (*volasertib* versus *saracatinib* versus *volasertib + saracatinib = 37* vs. *34* vs. *47 days; p=0.0019, log-rank test*).

STAT3 inhibits apoptosis by activating transcription of anti-apoptotic effectors in the nucleus and by preventing opening of the mitochondrial permeability transition pore (MPTP) in the inner mitochondrial membrane.[9–12] Transcription of BCL-xL, one of these anti-apoptotic effectors, is stimulated by pY705 STAT3, and prevents calcium release through the MPTP. This not only blocks cytochrome *c* release, but it also maintains the mitochondrial membrane redox potential, which drives oxidative phosphorylation.[23] BCL-xL expression is significantly increased in resistant *Trp53/Pten(−/−)* GBM cells (Figure 2E). We suppressed BCL-xL in *Trp53/Pten(−/−)* ispinesib resistant and naive GBM cells with shRNA (Figure 2F) and counted cells after 5 days of transfection. BCL-xL suppression in ispinesib naive cells has no significant effect on cell count, while in resistant cells in the presence of 75 nM ispinesib, it reduces cell count by > 5-fold (*$p < 0.0001$, two-tailed t test*). BCL-xL can be inhibited by the BCL2 inhibitor navitoclax.[24] We therefore also examined whether navitoclax reverses resistance by measuring cell viability in the presence of combinations of navitoclax and spindle inhibitors and by fitting data to the synergy algorithm MuSyC.[25,26] MuSyC fits dose-response surfaces (Figures 2G–2I, *left*) to drug combination data to calculate the degree of synergistic efficacy (β) and synergistic potency (*log(α12) and log(α21)*). Combining navitoclax with each spindle inhibitor reduces GBM cell viability by > 2-fold compared to either drug alone (Figures 2G–2I, *right*, $\beta_{obs} > 1.0$) and reduces the $EC_{50}$ of one drug by the other between 7 and to250-fold

**Figure 1. Resistance to three spindle inhibitors works by a similar mechanism**

(A) Treatment of *Trp53/Pten(−/−)* murine GBM cells with ispinesib, alisertib, or volasertib leads to marked cellular and nuclear enlargement. Scale bar = 100 μm.
(B and C) Alisertib (B) and volasertib (C) resistant cells increase STAT3 phosphorylation at Y705 and S727 2- to 4-fold. Asterisks indicate pairwise *p* values, determined by a two-tailed t test.
(D–F) Src phosphorylation is enhanced 2- to 3-fold in alisertib and volasertib-resistant cells. Asterisks indicate pairwise *p* values, determined by a two-tailed t test.
(G–J) The expression of phosphorylated EGFR (G and H) total EGFR (G,I), and fractional EGFR phosphorylation (G, and J) increases 4- to 5-fold in spindle inhibitor resistance. Brackets indicate *p* values, determined by pairwise two-tailed t tests.
(K–M) Gene set enrichment analyses from bulk RNA-seq of alisertib and volasertib-resistant cells (K and L). Gold arrows denote upregulated gene ontologies related to STAT3, STAT5, TGFβ, apoptosis, and the epithelial-to-mesenchymal transition, and blue arrows denote downregulated ontologies related to mitotic spindle, $G_2M$, and MYC pathways.
(M) Of those genes upregulated with the development of resistance, nearly 3000 (53%) are shared between ispinesib, alisertib, and volasertib-resistant cells (M).

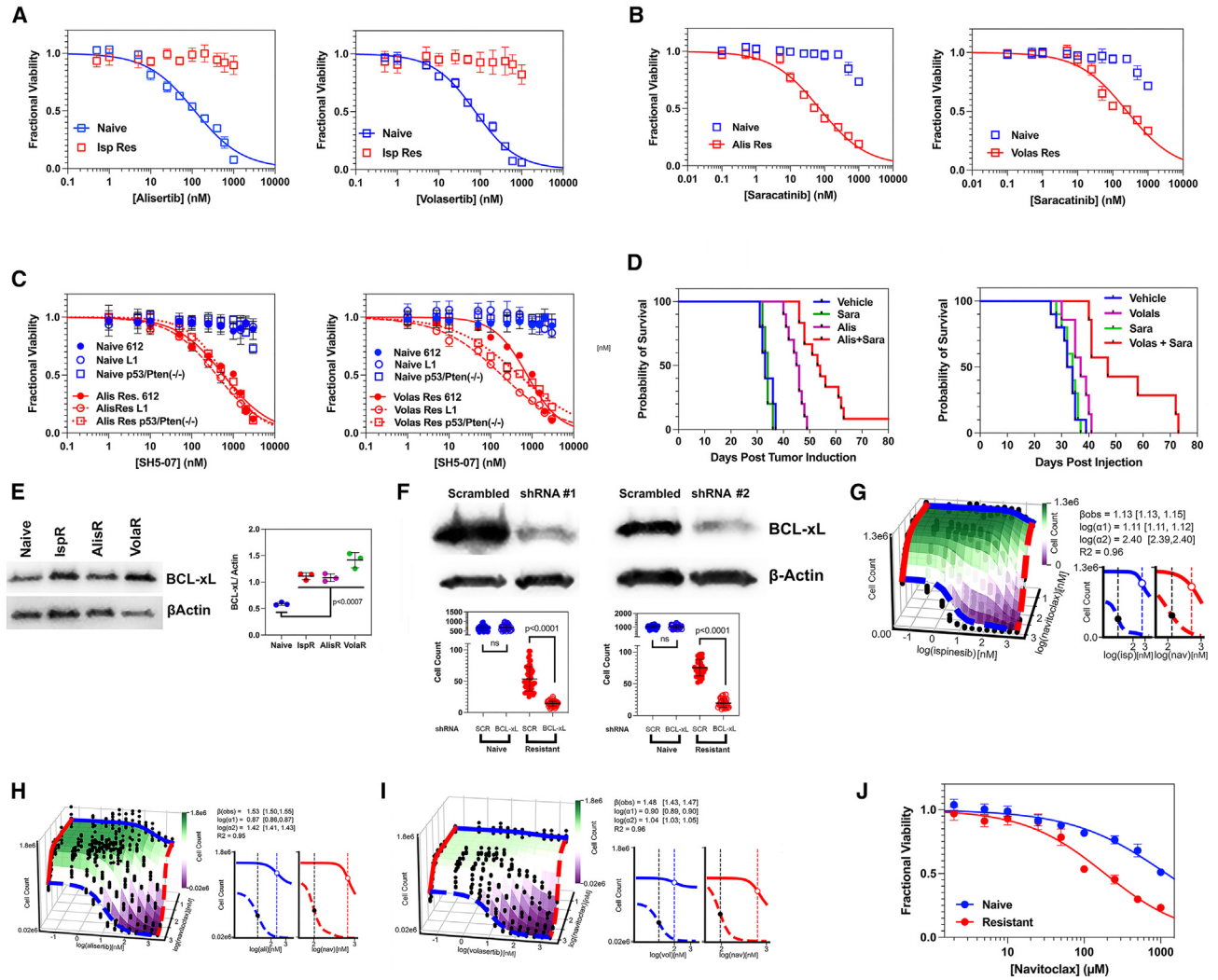


**Figure 2. GBM cells resistant to ispinesib, alisertib, and volasertib share therapeutic vulnerabilities**

(A) Ispinesib-resistant *Trp53*/*Pten*(−/−) murine GBM cells (*red*) are also resistant to alisertib (*left*) and volasertib (*right*).

(B) Resistance to alisertib (*left*) and volasertib (*right*) renders cells sensitive to saracatinib.

(C) While drug naive human 612 and L1 GBM cells and murine *Trp53*/*Pten*(−/−) cells (*blue*) are insensitive to the STAT3 inhibitor SH5-07, they become sensitive when resistant to alisertib (*left*) and volasertib (*right*).

(D) (*Left*). Kaplan Meier survival curves for *Trp53*/*Pten*(−/−) GEMMs treated with vehicle (*blue*), saracatinib (*green*), alisertib (*magenta*), or alisertib + saracatinib (*red*).

(E) Spindle inhibitor resistant *Trp53*/*Pten*(−/−) cells upregulate expression of BCL-xL 2- to 2.5-fold.

(F) shRNA suppression of BCL-xL by >90% (*left*) has no effect on the viability of naive cells (*blue*), compared to scrambled shRNA (SCR), but reduces cell count in ispinesib resistant cells by > 5-fold (*red*). *p* values determined with a two-tailed t test.

(G–I) (*Left*) Dose-response surfaces for the combinations of navitoclax with ispinesib (G), alisertib (H), and volasertib (I) in resistant *Trp53*/*Pten*(−/−) cells. The cell count for each pair of drugs (*black dots*) was fit to the MuSyC equation (*surface plot*), with synergistic combinations denoted by the magenta shading. Values in brackets represent the 95% confidence intervals for the synergy parameter fits.

(J) Navitoclax dose responses for naive (*blue*) and ispinesib resistant (*red*) cells in the absence of ispinesib. *p* values determined by pairwise two-tailed t tests.

(Figures 2G–2I, *right*, *log(α12) and log(α21) between. 0.87-2.4*). In particular, MuSyC analysis indicates that navitoclax has an $EC_{50}$ of ∼250 nM in ispinesib resistant cells at vanishingly low ispinesib concentrations (*>100-fold less than the ispinesib $EC_{50}$,* Figure 2G, *left panel, solid red curve*) If resistance is stable once formed, we would therefore predict that if we make GBM cells ispinesib resistant and then remove ispinesib, they should retain their navitoclax sensitivity with an $EC_{50}$ of ∼250 nM. We tested this by performing a dose response of navitoclax in naive cells and in ispinesib resistant cells in the absence of ispinesib (Figure 2J). While the $EC_{50}$ of navitoclax in naive cells is 1180 ± 84 nM, it drops >6-fold for resistant cells in the absence of ispinesib, to 186 ± 10 nM—remarkably close to the value of 250 nM predicted by our MuSyC analysis.

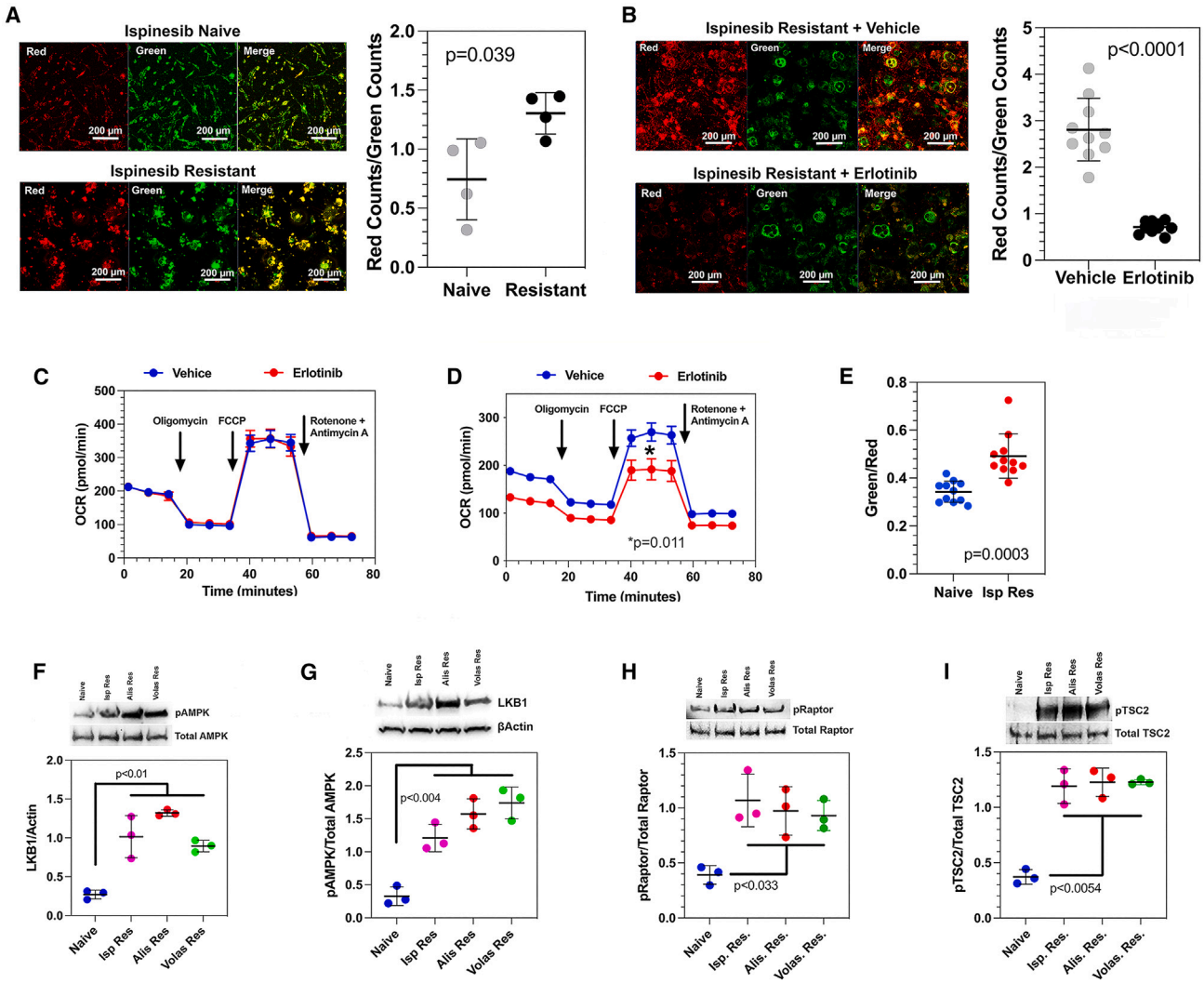


**Figure 3. Resistance to spindle inhibitors induces metabolic re-programming**

(A) JC1 staining of drug naive (*left, top*) and ispinesib resistant (*left, bottom*) *Trp53/Pten*(−/−) murine GBM cells. Resistance leads to a nearly 2-fold increase in the red to green fluorescence ratio (*right*). Scale bar = 200 μm.

(B) Compared to vehicle (*left, top*), treatment of ispinesib resistant cells with erlotinib reduces mitochondrial redox potential to levels seen in drug naive cells (*right*). Scale bar = 200 μm.

(C and D) Oxygen consumption rate (OCR) for drug naive *Trp53/Pten*(−/−) murine GBM cells (C) and for ispinesib resistant cells (D) in the presence of vehicle (*DMSO, blue*) or 500 nM erlotinib (*red*). Error bars represent ±1 SEM.

(E) Compared to naive cells (blue), ispinesib resistance (red) increases mitochondrial ROS, by 43%.

(F–I) Resistance to spindle inhibitors increases expression of *p*-AMPK (F), *p*-LKB1(G), p-Raptor (H), and *p*-TSC2 (I). *p* values determined by pairwise two-tailed t tests.

## Resistance to spindle inhibitors induces metabolic re-programming

The increase in pS727 STAT3 content with spindle inhibitor resistance predicts that resistance will increase mitochondrial membrane potential, oxidative phosphorylation, and oxygen consumption rate (OCR). Furthermore, EGFR inhibition with erlotinib should reverse these resistance-induced increases by dephosphorylating S727. We measured mitochondrial membrane potential with JC1, a voltage-sensitive mitochondrial fluorophore whose emission shifts from green to red as the mitochondrial inner membrane becomes hyperpolarized. Ispinesib resistance increases the red/green fluorescence ratio nearly 2-fold (Figure 3A). Treatment with 500 nM erlotinib for 24 h reduces this ratio to that of naive cells (Figure 3B). While erlotinib has no significant effect on OCR in drug naive cells (Figure 3C), it reduces maximum OCR by ∼40% in ispinesib resistant cells (Figure 3D, *p=0.011, two-tailed t-test*). Reactive oxygen species (ROS) are a byproduct of oxidative phosphorylation, and we would predict that resistance increases mitochondrial ROS. We stained naive and ispinesib resistant cells with MitoCLox,

a mitochondrial localized fluorophore whose emission shifts from red to green with ROS, and found that the green/red intensity ratio increases in resistant cells by 43% (Figure 3E, $p = 0.0003$, *two-tailed t-test*).

GBM cells chronically treated with alisertib reverse the Warburg effect by increasing their reliance on oxidative metabolism for energy production.[27] These metabolic changes are accompanied by a reduction in c-MYC, which regulates the Warburg effect.[28] It was proposed that this reflects the loss of active Aurora Kinase A, which binds to c-MYC and protects it from proteasomal degradation. We therefore examined how resistance to ispinesib, alisertib, and volasertib affect levels of c-MYC. In each case, resistance leads to an 8- to 10-fold reduction in c-MYC expression (Figures S2A and B), consistent with our GSEA analyses (Figures 1K and 1L). Furthermore, we find that for each inhibitor, resistance leads to a 3- to 4-fold reduction in Aurora Kinase A expression (Figure S2C).

STAT3 enhances expression of liver kinase B1 (LKB1) and LKB1 activates AMP kinase (AMPK).[29] For each spindle inhibitor, resistance leads to a ~4-fold increase in LKB1 and pAMPK, as well as in two AMPK downstream effectors—TSC2 and Raptor (Figures 3F–3I). These findings suggest that STAT3 drives an integrated metabolic response in resistant cells that include enhancement of energy substrate import, through pY705 STAT3 induced transcription of LKB1, and of oxidative phosphorylation through pS727 STAT3 activation of complexes I and II of the ETC.

## Spindle inhibitor resistance and the mesenchymal phenotype reflect a role of STAT3 in both

These results lead us to predict that naive tumor cells that upregulate pY705 and pS727 STAT3 should *a priori* be more resistant to spindle inhibitors than naive cells that do not. Furthermore, STAT3 is one of two master transcriptional regulators of the mesenchymal phenotype in GBM,[30] implying that the well-established link between the mesenchymal phenotype and therapy resistance[31–33] may be mediated by STAT3. While drug naive *Trp53*/*Pten*(−/−) cells have a proneural signature, resistance not only to ispinesib,[9] but also to alisertib and volasertib leads to a proneural-to-mesenchymal shift (Figure S3). We examined the status of STAT3 phosphorylation in four drug naive GEMM GBM lines. Two of these, MES1861 and MES4622, are mesenchymal,[34,35] and the other two (PN20 and PN24) are Proneural.[36,37] The content of both pY705 STAT3 and S727 STAT3 is 4- to 5-fold higher in the MES lines (Figures 4A–4C), and this correlates with a 20- to 50-fold increase in the $EC_{50}$ of the three spindle inhibitors compared to the PN lines (Figures 4D–4F and Table S1). Suppressing STAT3 with shRNA by >90% (Figure S4) in the two mesenchymal lines reduces the $EC_{50}$ for each spindle inhibitor 30- to 50-fold (Figures 4G–4I and Table S1), to values that are similar to those for the two proneural lines.

## Resistance to spindle inhibitors is accompanied by therapy induced senescence

The cellular and nuclear enlargement in resistant GBM cells (Figure 1A) has also been described in TIS.[38] While drug naive cells are nearly uniformly negative for the senescence marker β-gal (A), approximately 50–60% of ispinesib, alisertib, and volasertib resistant cells are positive (Figure 5B). Likewise, resistance to each inhibitor leads to downregulation of lamin B and upregulation of p21 (Figures 5C–5E)—two additional senescence markers.[39,40] Resistance to each inhibitor in *Trp53*/*Pten*(−/−) GBM cells produces a 4- to 6-fold increase in the fraction of cells with high forward and side scatter by flow cytometry (Figure 5F), similar to previous reports in TIS.[38] To determine if these enlarged cells have undergone TIS, we treated both naive and resistant cells with the fluorescent β gal substrate FDGlu, and performed flow cytometry (Figures 5G and S5A). We plotted the fraction of total cell counts that had high side (Figure 5F) or forward scatter (Figure S5A) and were either β-gal+ (*closed circles*) or β-gal- (*open circles*). We found that nearly all resistant cells with high side and forward scatter (Figures 5H and S5B) are β gal +, while among those with low side (Figure 5I) or forward scatter (Figure S5C) a substantial fraction is also β gal +. This suggests that development of TIS in resistant GBM cells precedes and/or can occur independently of increases in cell size or complexity. We observe similar results a human GBM cell line (L1, Figure S6).

If the TIS subpopulation depends on phosphorylation of STAT3 at Y705 and S727 to prevent apoptosis, then treating resistant tumors with saracatinib should deplete them. We generated ispinesib resistant *Trp53*/*Pten*(−/−) cells, replaced ispinesib with either vehicle (DMSO) or 500 nM saracatinib for four days, and stained them with DAPI, rhodamine phalloidin, and FDGlu. Results are illustrated in Figure 5J and 5K. They confirm that saracatinib reduces the fraction of β-gal + cells approximately 5-fold. Treating these resistant cells with saracatinib also induces caspase 3 cleavage, implying that saracatinib induces apoptosis in TIS cells (Figures 5L and 5M). We treated *Trp*53-deleted GEMMs *in vivo* with vehicle, ispinesib, or with three weeks of ispinesib followed by one week of saracatinib, and examined the brains histologically with H&E and for p21. Results are illustrated in Figures 5N–5P. While vehicle treated tumors are relatively uniform in size (Figure 5N, *top*), approximately 50% of cells in ispinesib treated tumors contain a substantial fraction of cells with enlarged or multiple nuclei, along with occasional monopolar spindles, a cytological hallmark of ispinesib treatment (Figure 5O, *top, white arrow*). These large cells, however, are not apparent in tumors treated sequentially with ispinesib for three weeks followed by saracatinib for one week (Figure 5P, *top*). While vehicle treated tumors show sparse staining for p21 (Figure 5N, *bottom*), ispinesib increases the p21+ subpopulation significantly (Figure 5O, *bottom*). However, treating with ispinesib for three weeks followed by saracatinib for one week eliminates the vast majority of the p21+ cells (Figure 5P, *bottom*).

## TIS cells are central to the process of spindle inhibitor resistance

Treating ispinesib resistant GBM cells with maximal doses of saracatinib alone eliminates only ~50% of cells.[9] Eliminating 100% of resistant cells requires combining saracatinib with ispinesib. This suggests that resistant GBMs contain at least two subpopulations—a TIS subpopulation that uses STAT3 to suppress apoptosis and is sensitive to saracatinib, and another that resists ispinesib in some other way and is saracatinib insensitive. Since spindle inhibitors are only active in $G_2M$, tumor cells

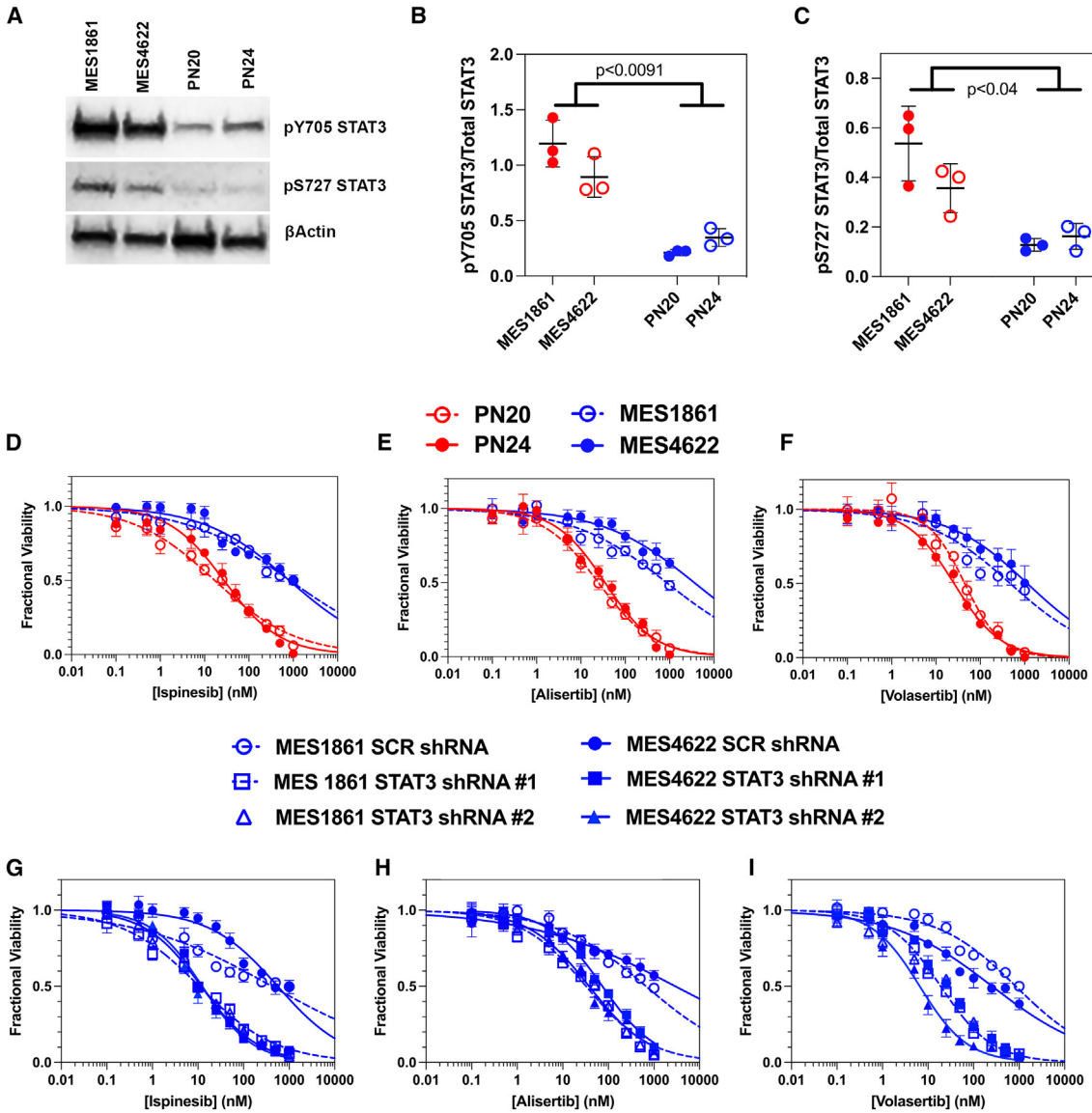


**Figure 4. STAT3 activation connects therapy resistance with the mesenchymal phenotype**

(A–C) Levels of pY705 STAT3 and pS727 STAT3 are increased 4- to 5-fold in two mesenchymal GEMM lines (MES1861 and MES4622) compared to two proneural GEMM lines (PN20 and PN24).

(D–F) MES1861 and 4622 lines (*blue*) have $EC_{50}$ values for ispinesib (D), alisertib (E), and volasertib (F) that are 40- to 50-fold higher than for two proneural lines (*red*).

(G–I) shRNA suppression of STAT3 in the MES1861 and 4622 lines reduces the $EC_{50}$ for ispinesib (G), alisertib (H), and volasertib (I) by 40- to 50-fold. See also Table S1 *p* values determined by pairwise two-tailed t tests.

could also resist these drugs by entering quiescence. Quiescence in GBM can be induced by TGFβ and reversed with SB431542, a TGFβ receptor inhibitor.[21] The TGFβ signaling pathway is upregulated in GBM cells resistant to ispinesib,[9] alisertib, and volasertib (Figures 1K and 1L), and TGFβ is a component of the SASP.[17,18,38]

TIS cells can undergo DNA replication by entering the cell cycle at S phase, exiting at $G_2M$ and re-entering at S phase in a process referred to as *endoduplication*, which leads to nuclear enlargement and multinucleation.[41,42] Furthermore, under some circumstances, including loss of *Trp53*[43] or withdrawal of chemotherapy,[44] TIS cells can become proliferative. Regardless, either process can explain why both Ki67, which stains cells in G1, S, and $G_2M$, and EdU, which stains cells in S phase, can both be detected *in vitro* in ispinesib resistant *Trp53*(−/−) GBM cells (Figure 6A). In both cases, we observe staining in the large nuclei, characteristic of TIS cells. We also treated orthotopic, *Trp53*(−/−) GEMMs with vehicle (DMSO) or ispinesib for three weeks and processed the brains for H&E and immunohistochemistry for Ki67. Both vehicle and ispinesib treated tumors stain

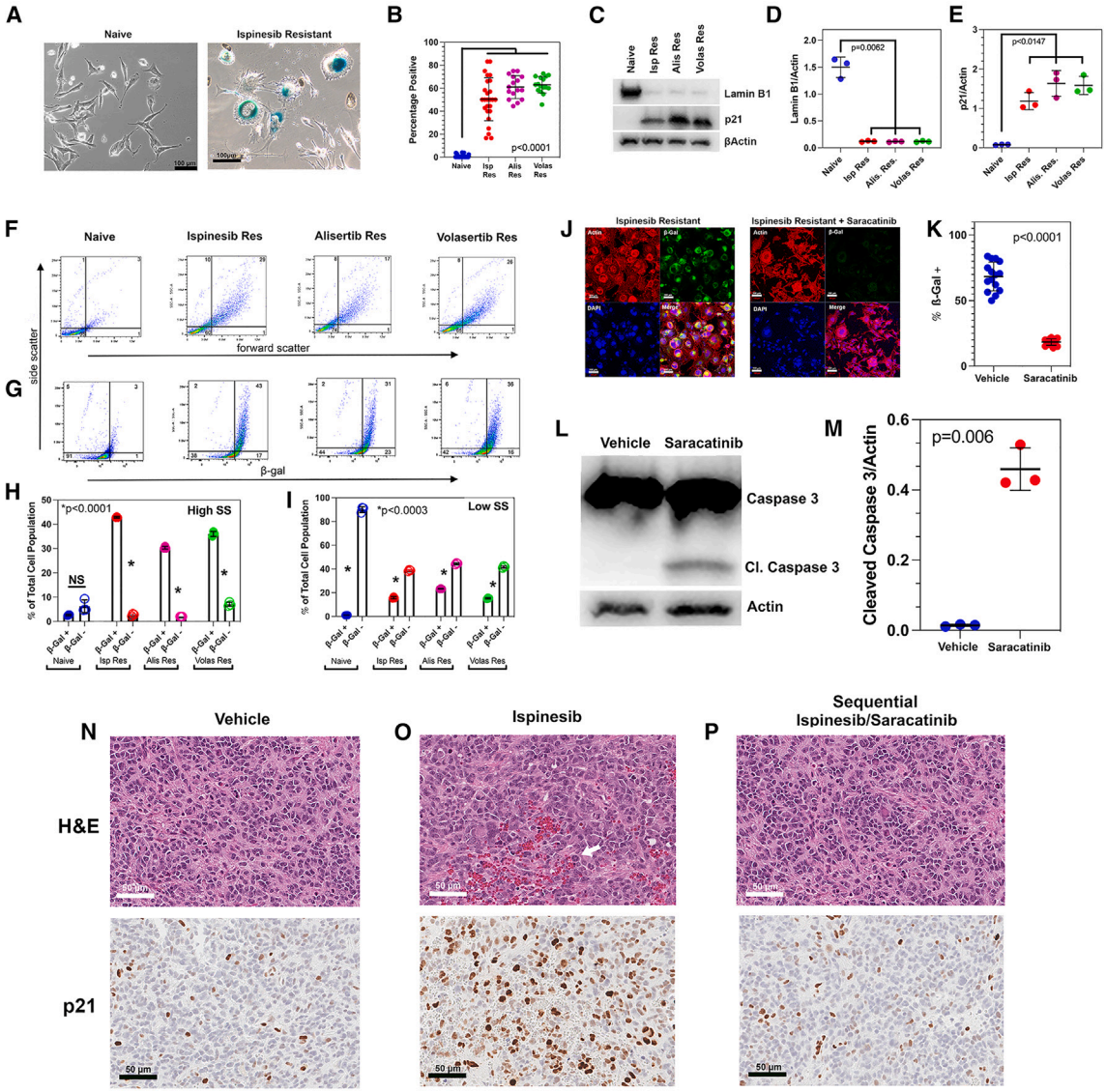


**Figure 5. Resistance to spindle inhibitors is accompanied by accumulation of TIS tumor cells**

(A) While naive cells are β-gal negative, the large cells in an ispinesib resistant population stain positively. Scale bar = 100 μm.

(B) β−gal positivity is seen in approximately 50% of ispinesib, alisertib, and volasertib resistant cells. Brackets indicate pairwise *p* values, determined by a two-tailed t test.

(C–E) Cells resistant to each anti-mitotic down regulate lamin B1 and upregulate p21. Asterisks indicate pairwise *p* values, determined by a two-tailed t test.

(F) Forward versus side scatter flow cytometry of naive and resistant *Trp53*/*Pten*(−/−). Numbers in each quadrant represent the mean percentages of the total signal.

(G) Naive and resistant cells were stained with FDGlu and subjected to flow cytometry to measure side scatter versus β-galactosidase activity.

(H) Bar plot depicting the fraction of the total cell population that demonstrates both high side scatter and either positive or negative β-gal activity.

(I) Bar plot depicting the fraction of the total cell population that demonstrates both low side scatter and either positive or negative β-gal activity. Asterisks in H and I indicate pairwise *p* values, determined by a two-tailed t test.

(J) (*Left*) Ispinesib resistant *Trp53*(−/−) cells were stained for actin (*red*), FDGlu (*green*), or DAPI (*blue*). (*Right*) Removal of ispinesib and treatment with 500 nM saracatinib for 72 h demonstrates near complete loss of β-gal + cells. Scale bar = 100 μm.

(K) Saracatinib treatment reduces the fraction of cells positive for β-gal activity by > 5-fold.

(L and M) Saracatinib treatment of ispinesib resistant cells leads to caspase 3 cleavage. *p* value determined by two-tailed t test.

(N–P) GEMMs with orthotopic *Trp53*(−/−) tumors were treated with vehicle, ispinesib x 3 weeks, or with ispinesib x 3 weeks followed by one week of saracatinib. H&E-stained tumor sections reveal that while vehicle treated tumors are composed of cells with relatively uniform size (N*, top panel*), ∼40% of cells in ispinesib treated tumors have enlarged or multiple nuclei (O*, top panel*). These cells disappear in tumors treated with ispinesib for three weeks followed by saracatinib for one week (P, *top panel*). Immunohistochemical staining for p21 demonstrates sparse staining in vehicle treated mice (N, *bottom*). Ispinesib markedly increases the number of p21+ cells (O, *bottom*), while subsequent treatment with saracatinib reduces this number to levels similar to vehicle (P, *bottom*). Scale bar = 50 μm.

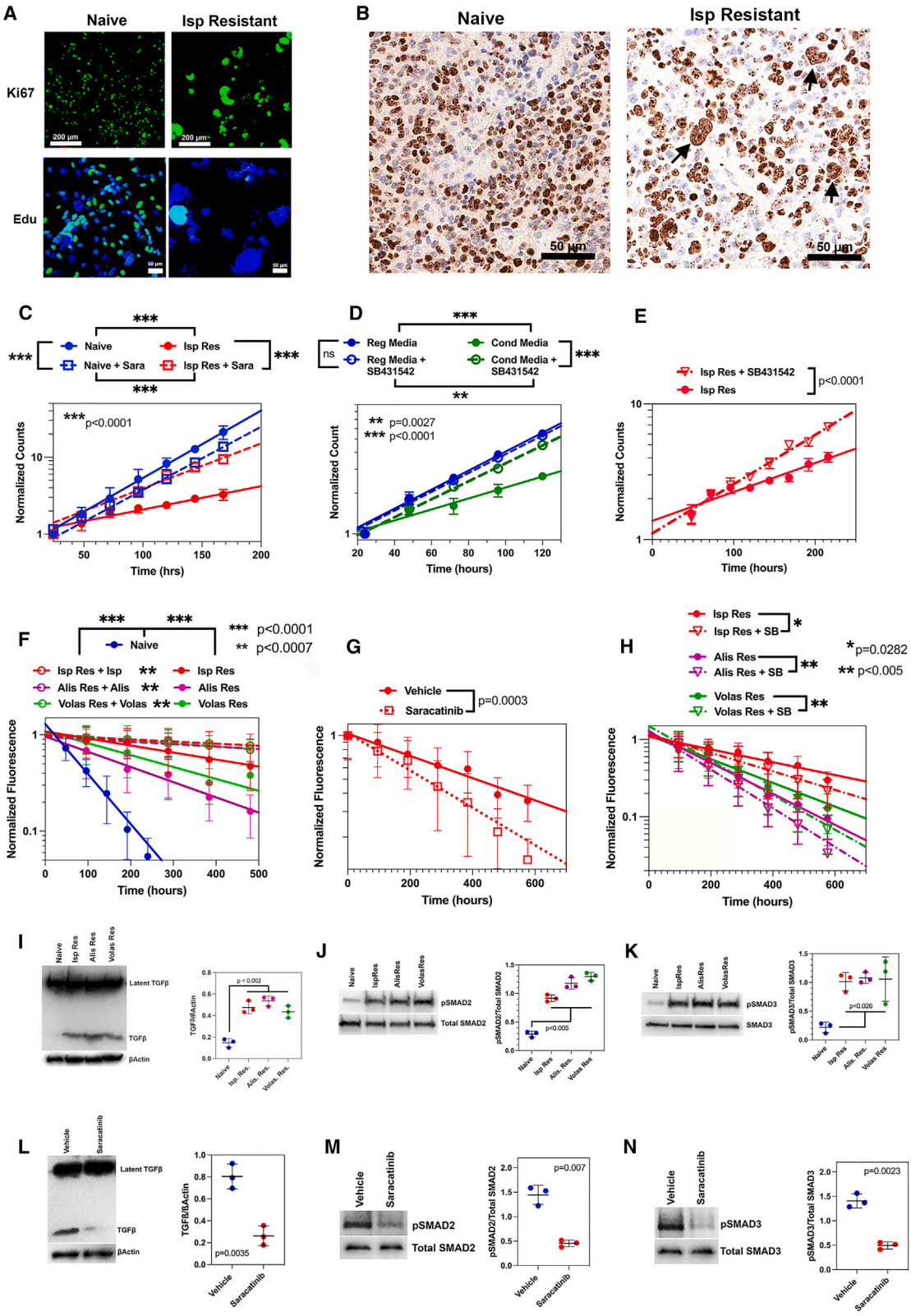


*(legend on next page)*

robustly for Ki67 (Figure 6B), with Ki67 staining seen in ispinesib-treated tumor cells with enlarged nuclei (*black arrows*).

We measured the proliferation rate of naive and ispinesib resistant*Trp53/Pten*(−/−) cells in the absence of ispinesib, using an ATP dependent assay (*CellTiter Glo*) and fit the data to single exponential growth curves. Data are depicted as the solid blue and red lines in the semi-logarithmic plot in Figure 6C. The rate constants for these fits demonstrate that ispinesib resistant cells proliferate ∼4-fold more slowly than naive cells (Table S2). While treating naive tumor cells with saracatinib reduces proliferation rate by <7% (Figure 6C; *blue open boxes/dashed line*; Table S2), it paradoxically accelerates proliferation in ispinesib resistant cells (Figure 6C, *red open boxes/dashed line*; Table S2) nearly 2-fold, suggesting that eliminating TIS cells releases mitotic suppression of one or more of the remaining subpopulations.

To test if this suppression of is due to paracrine factors, we compared the proliferation kinetics of drug naive cells under two conditions—in unconditioned media (*regular media* in Figure 6D) and in media conditioned by exposure to ispinesib resistant cells (*conditioned media* in Figure 6D). Compared to regular media (Figure 6D, *solid blue circles and line*), conditioned media (Figure 6D, *solid green circles and line*; Table S2) slows proliferation by >80%. While SB431542 has almost no effect on the proliferation of naive cells (Figure 6D, *open blue circles, dashed blue line*; Table S2), it accelerates proliferation of these cells when cultured in conditioned media by ∼70% (Figure 6D, *open green circles, dashed green line*; Table S2). We also find that SB431542 accelerates proliferation of ispinesib resistant cells by ∼70% (Figure 6E, *dashed* vs *solid red lines*; Table S2).

Resistance is associated with increased oxidative metabolism (Figure 3) which leads to increased ATP production, and this could complicate the interpretation of proliferation data using an ATP-dependent assay. We therefore also used a second method to measure proliferation, which involves transfection of drug naive *Trp53/Pten*(−/−) murine or L1 human GBM cells with a lentiviral vector encoding an H2B-GFP fusion protein under transcriptional control of the doxycycline promoter. Briefly treating with doxycycline to induce H2B-GFP expression and then removing it leads to loss of GFP fluorescence over time due to its serial dilution in generations of proliferating daughter cells. An example is depicted in Figure S7A for drug naive and resistant L1 cells. Fluorescence intensity data were fit to single exponential decays to yield apparent rate constants for proliferation, summarized in Table S2 for *Trp53/Pten*(−/−) murine and in Table S3 for L1 human GBM cells. Although there are differences between corresponding rates for the ATP-dependent and H2B-GFP pulse-chase methods, both show that the proliferation of resistant cells in the absence of spindle inhibitor is ∼3- to 4-fold slower than for naive cells (Figures 6F and S7B), and that both saracatinib (Figure 6G) and SB431542 (Figures 6H and S7C) accelerate the proliferation of resistant cells. Furthermore, the proliferation of resistant cells in the presence of a spindle inhibitor is 5- to 15-fold slower than in its absence (Figures 6F and S7B, *dashed* versus *solid lines*).

These results imply that TIS cells can suppress proliferation in the non-TIS population through paracrine factors. In support of this, levels of active TGFβ as well as of two of its downstream effectors, SMAD2 and SMAD3, are 4- to 5-fold higher in resistant *Trp53/Pten*(−/−) cells cultured without spindle inhibitors than in drug naive cells (Figures 6I–6K). Treatment with saracatinib reverses these effects (Figures 6L–6N).

## The interactions between proliferative, quiescent, and TIS GBM cells support a sequential treatment strategy

Our results support the model depicted in Figure 7A. We propose that GBMs consist of proliferative, quiescent, and TIS subpopulations. While some proliferative cells are killed by spindle inhibitors, others activate STAT3 to suppress the apoptosis that typically follows a prolonged $G_2M$ block and enter a TIS state. TIS cells in turn suppress the conversion of quiescent to proliferative cells through components of the SASP, including TGFβ. We also propose that proliferative cells are in a reversible equilibrium with quiescent cells. Whether the TIS state can revert to the proliferative (*indicated by the thin arrow in* Figure 7A) or not, our model predicts that depleting proliferative cells with a spindle inhibitor will reduce the fraction of this subpopulation and increase the fraction of TIS cells. Conversely, killing TIS cells with saracatinib should reverse the TIS-induced block on the quiescent → proliferative transition, leading to a corresponding increase in the proliferative compartment.

**Figure 6. Resistance to spindle inhibitors involves cross talk between SASP components, including TGFβ, and proliferative, TIS, and quiescent tumor cells**

(A) (*Top Row*) Ki67 staining of drug naive *Trp53/Pten*(−/−) cells (*left*) and ispinesib resistant cells (*right column*) *in vitro*. Scale bar = 200 μm. *Bottom row:* drug naive (*left*) and ispinesib resistant (*right*) *Trp53/Pten*(−/−) cells were stained for EdU (*green*) to mark cells in S phase, and DAPI (*blue*) to highlight nuclei. Scale bar = 50 μm.

(B) Ki67 staining of GBMs from mice treated with vehicle (*left*) or ispinesib (*right*) for three weeks. In the ispinesib treated sample, Ki67 staining can be observed in cells with enlarged (*arrows*) nuclei.

(C–E) *In vitro* proliferation for *Trp53/Pten*(−/−) cells measured with an ATP-dependent assay (*CellTiter Glo*). (C) Proliferation of cells that are naive (*solid blue circles*), naive + saracatinib (*open blue boxes*), ispinesib resistant (*solid red circles*), and ispinesib resistant + saracatinib (*open red boxes*), fit to single exponential growth equations (*dashed and solid lines*), (D). Proliferation of drug naive cells in regular media (*solid blue circles*), regular media + SB431542 (*open blue circles*), conditioned media (*solid green circles*), and conditioned media + SB431542 (*open green circles*). (E). Ispinesib resistant cells in the absence of ispinesib were treated with vehicle (*solid blue circles*) or SB431542 (*open red triangles*).

(F and G) Measurement of proliferation using the kinetics of H2B-GFP washout. (F). Compared to drug naive cells (*blue*), cells resistant to ispinesib (*red*), alisertib (*magenta*), or volasertib (*green*) proliferate 2.5- to 5-fold more slowly in the absence of spindle inhibitors, and ∼16-fold more slowly in their presence. (G). Proliferation of ispinesib resistant cells in the absence of ispinesib is accelerated ∼70% by addition of saracatinib.

(H) Proliferation of ispinesib (*red*), alisertib (*magenta*), and volasertib (*green*) resistant cells in the absence of spindle inhibitor is accelerated 25–45% by addition of SB431542.

(I–K) Levels of active TGFβ (I), phospho SMAD2 (J), and phospho SMAD3 (K) are increased in cells resistant to ispinesib, alisertib, or volasertib.

(L–N) In ispinesib resistant cells, treatment with saracatinib significantly reduces active TGFβ (L), phospho SMAD2 (M), and phospho SMAD3 (N).

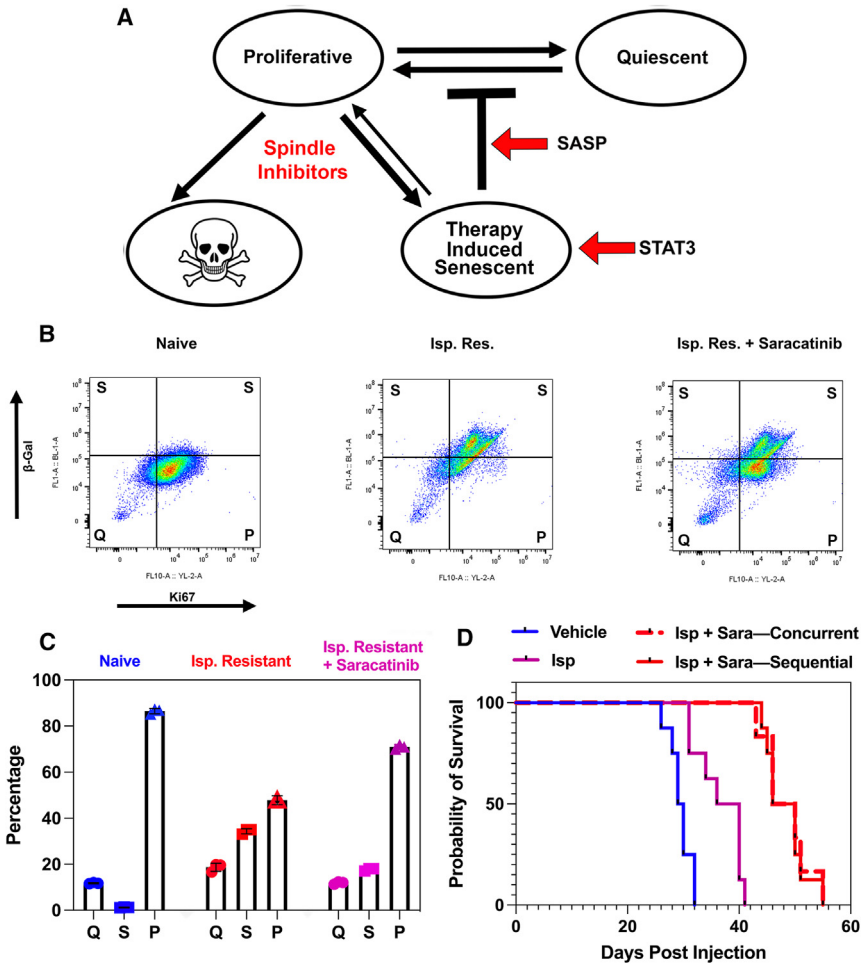


**Figure 7. The interactions between proliferative, quiescent, and TIS GBM cells support a sequential treatment strategy**

(A) Three cell state model for resistance to spindle inhibitors.

(B) Two color flow cytometry scatterplot of naive, ispinesib resistant, and ispinesib resistant +saracatinib treated *Trp53*(−/−) cells. Numbers in each quadrant represent the mean percentages of the total signal.

(C) Percentages of the total cell population that are quiescent (*left*), senescent (*center*), or proliferative (*right*), for naive (*blue*), ispinesib resistant (*red*), and ispinesib resistant treated with saracatinib for 48 h (*magenta*).

(D) GEMMs with orthotopic *Trp53*(−/−) GBMs were treated with vehicle (*blue*), ispinesib (*magenta*), ispinesib + saracatinib given concurrently (*red dashed*), or in alternating cycles of 3 weeks of ispinesib followed by 1 week of saracatinib (*solid red*).

We have tested these predictions by performing flow cytometry on three groups of *Trp53/Pten*(−/−) cells—naïve, ispinesib resistant, and ispinesib resistant treated with saracatinib for 48 h. Cells were stained with FDGlu, to mark β-gal + cells, and anti-Ki67, to mark cycling cells, and results are depicted in Figure 7B. The four quadrants in the two-dimensional scattergram correspond to the following: lower left: Ki67-and β-gal - (*quiescent*=**Q**); lower right: Ki67+ and β gal- (*proliferative*=*P*); upper left: Ki67-and β-gal+ (*therapy induced senescent*=***S***); and upper right: Ki67+ and β-gal+ (*therapy induced senescent cells undergoing DNA replication*=***S***). Figure 7C illustrates the percentage of **S** (*β-gal +, Ki67 + and -*), P, and **Q** subpopulations for naive (*blue*), ispinesib resistant (*red*) and ispinesib resistant + saracatinib (*magenta*) tumor cells. Ispinesib resistance reduces the fraction of proliferative cells ∼2-fold ($p=0.0017$, *two-tailed t test*); increases the fraction of TIS cells ∼10-fold ($p < 0.0001$, *two-tailed t test*), consistent with some of the former evolving into the latter; and increases the fraction of quiescent cells ∼30% ($p=0.0001$, *two-tailed t test*) Treating ispinesib resistant cells with a 48 h exposure to saracatinib reverses these effects.

Our model explains why saracatinib paradoxically stimulates proliferation in resistant cells but not in drug naive cells (Figures 6C and 6G), since reducing the TIS subpopulation with saracatinib would reduce SASP factors and release quiescent cells to proliferate. It also explains the survival benefit of combining spindle inhibitors with saracatinib (Figure 2D and Kenchappa et al.[9]), which would deplete the TIS subpopulation, enabling more quiescent cells to become proliferative and become spindle inhibitor sensitive. One problem with translating this approach clinically is that both spindle inhibitors and the *senolytics* saracatinib and navitoclax have overlapping toxicities, including myelosuppression.[45–48] However, administering the same doses of these two drugs in an alternating schedule might not only provide equivalent survival benefit with less toxicity, but also allow dose escalation of each drug beyond what could be tolerated when both are co-administered. As a first step to test this, we treated our *Trp53*(−/−) GEMMs with vehicle, ispinesib alone, concurrent ispinesib + saracatinib, or with repeated cycles of ispinesib for three weeks alternating with saracatinib for one week. The resulting Kaplan Meier curves (Figure 7D) show that the concurrent and sequential treatment schemes produce statistically indistinguishable survival benefits (*median survival 48 days, p=0.82, log-rank test*), which are both significantly better than ispinesib or vehicle alone ($p < 0.0005$, *log-rank test*).

## DISCUSSION

### Spindle inhibitor resistance works by a shared set of mechanisms and generates a shared set of vulnerabilities

Although ispinesib, alisertib, and volasertib inhibit distinct components of the mitotic spindle, resistance to each produces the same phenotype, including upregulation of nearly 3000 genes in common as well as cytomegaly and nuclear pleomorphism (Figure 1). This argues that the mechanism of resistance to these

drugs does not involve mutations that prevent drug binding to target and subsequent blocking of mitotic progression, a point we established previously with ispinesib resistance.[9] Rather, our data suggests that resistance works by blocking the apoptosis that ordinarily follows a prolonged $G_2M$ arrest. Furthermore, our finding that ispinesib resistance confers resistance to both alisertib and volasertib as well indicates that resistance to each inhibitor relies upon the same mechanism.

The gene sets enriched in resistant cells include those involved in the IL6-JAK-STAT3 pathway, which our prior scRNA-seq studies[9] found are uniformly upregulated in ispinesib-resistant murine *Trp53/Pten*(−/−) GBM cells, as well as those involved in apoptosis pathways. Among the latter is the anti-apoptotic protein BCL-xL, which is transcriptionally regulated by STAT3.[49] Our finding that the BCL-xL inhibitor navitoclax is highly synergistic with each spindle inhibitor supports our proposal that increasing the transcription of anti-apoptotic effectors is necessary for resistant GBM cells to survive. This conclusion is also supported by our results which show that STAT3 inhibition with saracatinib or SH5-07 is specifically cytotoxic to resistant cells.

## STAT3 activation explains the association of treatment resistance with the mesenchymal phenotype and metabolic reprogramming

An additional set of genes that are upregulated in resistant cells are those related to the epithelial-mesenchymal transition (EMT). EMT is frequently associated with development of resistance to chemotherapy and radiotherapy[50] and a similar proneural to mesenchymal shift has been associated with treatment resistance in GBM.[51] STAT3 and CEBPβ are the two master regulators of the mesenchymal phenotype in GBM,[30] and as we have shown (Figures 1B–1E *and* Kenchappa et al.[9]), activation of STAT3 and expression of the IL6-JAK-STAT3 pathway occurs with spindle inhibitor resistance. In addition, our bulk RNA-seq data demonstrate that CEBPβ is also upregulated in ispinesib, alisertib, and volasertib resistant cells (*Gene Expression Omnibus sequential accession numbers GSM8267005-GSM8267016*). We thus propose that activation of STAT3 underlies the association between resistance and the mesenchymal phenotype (Figures 2E–2H). While this suggests that mesenchymal GBMs are resistant to spindle inhibitors because of STAT3, it does not necessarily follow that all GBMs resistant to spindle inhibitors are mesenchymal. This is highlighted by our recent study[52] which showed that ispinesib resistance in TS543, a proneural human GBM line, does not lead to a proneural→mesenchymal shift. BCL-xL expression can be enhanced not only by STAT3, but also by other transcription factors, including MYB, which is upregulated in ispinesib-resistant TS543 cells.[53] This suggests that the final common pathway for spindle inhibitor resistance may involve anti-apoptotic proteins, including BCL-xL, whose expression is STAT3-dependent in tumors that upregulate STAT3, and STAT3 independent in some non-mesenchymal tumors.

Resistance induces metabolic changes designed to enhance energy production, including an increase in activated AMPK. Furthermore, resistance to both ispinesib (Figures 3A–3E) and alisertib[27] increases oxidative metabolism, which in the case of alisertib is driven by fatty acid oxidation. As we have shown, resistance to each of these spindle inhibitors also leads to TIS, and TIS in turn enhances lipid oxidation.[54] Resistance leads to a downregulation of $G_2M$ checkpoint and mitotic effectors (Figure 1K *and* Kenchappa et al.[9]) including Aurora Kinase A. If Aurora Kinase A protects c-MYC from proteasomal degradation,[27] then its downregulation with resistance (Figure S2C) could explain the loss of c-MYC that we observe, leading to a reversal of the Warburg effect and a shift toward a more oxidative metabolic profile.

## Therapy induced senescence accompanies the development of resistance

Like normal cells that undergo senescence during aging, tumor cells that undergo TIS express senescence markers, such as β−galactosidase and p21, and suppress expression of lamin B1. Furthermore, like their normal counterparts, TIS cells are deleterious, as they produce immunosuppressive, angiogenic, and stemness supporting effectors as part of the SASP.[15] However, analogies between normal and malignant cells only go so far. For example, while p53 is needed for senescence in aging, it is not for malignant cells in a TIS state. Likewise, as noted above, TIS cells can remain Ki67 and EdU+ by replicating their DNA through endoreduplication or by reverting to a proliferative phenotype.[42,55–58] As with STAT3 and the mesenchymal phenotype, the development of TIS on the one hand and of large size and complexity on the other may not be strictly linked, since flow cytometry shows that development of TIS can precede these morphologic changes (Figures 5A–D, S5, and S6).

Our data supports a model (Figure 7A) in which TIS cells are the main orchestrators of anti-mitotic resistance. We propose that they accomplish this first by surviving prolonged $G_2M$ arrest through the anti-apoptotic and metabolic effects of STAT3. Based on our prior DNA barcoding and scRNA-seq studies,[52] we also posit that TIS cells are stable and persistent, even after anti-mitotic is removed, and remain so both *in vitro* and *in vivo*. Through their STAT3-mediated survival, TIS cells also play active role in expanding the repertoire of resistant cells in a GBM. They accomplish this at least in part by secreting the SASP, which we have shown expands the resistant phenotype in the tumor cell population by enhancing retention of quiescent cells in a process driven at least in part by TGFβ. Given that the SASP contains multiple components that may also be contributing to tumor resistance, attempting to reverse resistance by targeting the SASP to overcome anti-mitotic resistance would be impractical. Rather, we propose that eliminating TIS cells is a strategy that gets to the source of the problem and can be accomplished by targeting STAT3 or at least one of its downstream anti-apoptotic effectors, BCL-xL.

## Resistance to spindle inhibitors in GBM can be described by a three-cell state model that has translational ramifications

GBMs consist of dynamic cellular subpopulations, and this has led to classification schemes that sort GBM cells into subgroups based on their lineage resemblance or functionality.[59–62] Nevertheless, one feature common to all of these is proliferation. For example, one scheme[60] described four subgroups, two of which

(*astrocyte-like and mesenchymal-like*) are considerably less proliferative than the other two (*NPC-like and OPC-like*). Likewise, one subgroup in another classification scheme[62] is distinguished from the others by its strong proliferative signature. Thus, sorting GBM cells into proliferative and or non-proliferative subgroups is consistent with each of these schemes. In our model of resistance, we further subdivide the non-proliferative subgroups into quiescent and TIS, which should both resist spindle inhibitors. These considerations lead to the three-cell state model in Figure 7A, whose salient features are supported by both our *in vivo* (Figures 6A and 6B) and *in vitro* (Figures 7B and 7C) data.

The effect of resistance on cell growth is relatively durable, since proliferation rates after removal of spindle inhibitors are ~4-fold slower than for naive cells (Figures 6C, 6F, and S7B). However, in the presence of spindle inhibitors, these rates become ~15- to 20-fold slower than drug naive cells (Tables S2 and S3). We propose that these growth rates represent an ensemble average of three intrinsic rates: the growth rate of proliferative cells and the rates of conversion of quiescent and TIS cells to proliferative cells. In the presence of spindle inhibitors, the population of proliferative cells drop, since some are killed by the drug and others develop TIS. In this case, cell growth rate would be largely determined by the transition rate from the TIS to the proliferative state. If so, our results would suggest that this would be an uncommon event, accounting for the overall very slow proliferation rate that we observe (Tables S2 and S3*; thin arrow in* Figure 7A). With the removal of spindle inhibitor, any cells remaining in the proliferative compartment could grow unimpeded. However, the number of cells in this compartment would be appreciably smaller than for naive cells, due to their depletion by prior exposure to spindle inhibitor (Figure 7C); and this would reduce the value of the overall, ensemble averaged growth rate. Furthermore, conversion of quiescent cells to proliferative would still be blocked by the presence of TIS cells. This would result in an overall growth rate that is still slower than the original, drug naive population.

Given its effects in eliminating TIS cells, saracatinib could be considered a "senolytic". However, not all senolytics are equally effective in all contexts. This is highlighted by our prior study[9] which showed that dasatinib, an SRC family kinase inhibitor which is generally regarded as a senolytic,[63] is ineffective in reversing ispinesib resistance by itself. Further, we showed that while saracatinib inhibits EGFR as well as SRC, dasatinib does not; and while dasatinib inhibits phosphorylation of STAT3 at Y705 it does not alter EGFR-mediated phosphorylation at S727. However, combining dasatinib with the EGFR inhibitor erlotinib is as effective as saracatinib in reversing ispinesib resistance. Our results emphasize that whether a drug is a senolytic or not is context dependent, and requires an understanding of how resistance and TIS develop and are maintained on a case-specific basis.

We would predict that alternating dosing of a spindle inhibitor with an appropriate senolytic should also be effective, as our model suggests that the TIS state is relatively stable. While treating with a spindle inhibitor would eliminate a large fraction of proliferating cells, it would still allow TIS cells to block quiescent cells from entering the cell cycle and repopulating the proliferative compartment. Following with a senolytic would then reduce the TIS population, induce quiescent cells to become proliferative, and in the process expand the population of cells that are sensitive to spindle inhibitors. One potential problem with alternating between drugs that inhibit different targets is that this approach may allow the tumor to evolve when the first drug is replaced by the second, due to activation of bypass pathways which neutralize the efficacy of the first drug.[64] However, two features argue against this concern. First, we find that prolonged treatment of GBM cells with ispinesib, alisertib, or volasertib produces a stable phenotype characterized by nuclear atypia and cytoplasmic enlargement. While the large/complex cells from resistant tumors may be able to remain in the cell cycle, they do not appear to revert to a normal mitotic phenotype, which we would have expected if alternative pathways that produce normal mitosis were activated. Second, alternating between ispinesib and saracatinib is no less effective than simultaneously treating with both drugs (Figure 7D). In addition to protecting tumor cells from the cytotoxicity of spindle inhibitors, TIS cells also support tumor progression by suppressing anti-tumor immunity. This point is highlighted by our finding that TIS cells produce activated TGFβ, a well-documented immunosuppressant[65] (Figures 6I–6N). Thus, although TIS cells may be responsible for slowing tumor growth, they nonetheless enhance tumor lethality in multiple ways. We propose that our approach to understanding how TIS and STAT3 drive resistance may apply to the development of resistance to other cytotoxic/cytostatic therapies, and it should be instructive in designing treatment schemes that both optimize efficacy and reduce toxicity to improve patient outcome in glioblastoma.

## Limitations of the study

Our work has extended our prior results by showing that STAT3 is the driving mechanism not only behind resistance and not only for ispinesib but also for two other targeted $G_2M$ inhibitors, alisertib and volasertib. However, our work does not rule out the possibility that resistance is a more complex process that is modulated by other, established resistance mechanisms, such as efflux transporters, that are also upregulated in inhibitor resistant cells and which can be targeted pharmacologically. Furthermore, this study does not address the effects or SASP components on the immune microenvironment in GBM, and the role lymphoid and myeloid cells play in contributing to the resistant phenotype. Furthermore, while studies with mouse models used equal numbers of male and female mice, our studies were not powered to determine the role of sex as an independent variable. Finally, while STAT3 regulates expression of a variety of anti-apoptotic effectors, other transcription factors do so as well, and it remains possible that some GBM tumors rely on STAT3-independent forms of apoptosis suppression to maintain the viability of TIS cells. Exploring this possibility will require a systematic examination of multiple GBM models in studies outside the scope of this current work.

## RESOURCE AVAILABILITY

### Lead contact

Further information and requests for resources and reagents should be directed to and will be fulfilled by the lead contact, S.S.R. (rosenfeld.steven@mayo.edu).

### Materials availability

Genetically engineered mouse models and cell lines will be distributed after completion of the relevant Materials Transfer Agreements with the Mayo Clinic.

### Data and code availability

- Data: Bulk RNA-seq data have been deposited in the Gene Expression Omnibus (GEO) database and are publicly available as of the date of publication. The accession number is listed in the key resources table
- Code: This paper does not report any original code.
- All other items: Any additional information required to reanalyze the data is available from the lead contact upon request.

## ACKNOWLEDGMENTS

SSR is supported by NIH grants NS073610, NS118513, NS119714, and CA210910, and by a Translational Adult Glioma Award from the Ben and Catherine Ivy Foundation. P.C. is supported by NIH grants NS073610 and NS118513. PAS is supported by NIH grant NS118513. R.S.K. is supported by NIH grant NS118513. C.T.M. was supported by K99/R00 Pathway to Independence Award from NIAID (1K99AI175656).

We wish to thank Dr. Justin D. Lathia (Lerner Research Institute of the Cleveland Clinic Foundation) for his gift of L1 cells, Drs. Alfredo Quiñones-Hinojosa and Hugo Guerrero-Cazares (Mayo Clinic Florida) for their gift of GBM612 cells, Dr. Roland Friedel (Mount Sinai School of Medicine) for his gift of SD2 and SD3 cells and for technical advice, Drs. Loic Deleyrolle (University of Florida) and Terrence Burns (Mayo Clinic Rochester) for helpful discussions; and Ms. Trine Giaever for her graphical abstract.

## AUTHOR CONTRIBUTIONS

Conception and design: R.K., A.D., N.Z., S.R., and P.C.; Development of methodology: R.K., A.D., C.T.M., S.R., P.C. Acquisition of data: R.K., N.Z., A.D., V.D.A.F., A.H., N.K.H.N. Analysis and interpretation of data: R.K., N.Z., V.D.A.F., A.D., P.A.S., C.T.M., P.C., D.H., and S.R.

## DECLARATION OF INTERESTS

Christian T. Meyer is a co-founder and part equity holder in Duet BioSystems. Steven S. Rosenfeld is a member of the External Advisory Board of Myosin Therapeutics and is part equity holder in this company. The authors declare no competing interests.

## STAR★METHODS

Detailed methods are provided in the online version of this paper and include the following:

- KEY RESOURCES TABLE
- EXPERIMENTAL MODEL AND STUDY PARTICIPANT DETAILS
  - Mice
  - Cell lines
- METHOD DETAILS
  - Glioma cell line isolation from mouse GBM tumor and culture
  - Dose-response curves/cell viability assays
  - Retrovirus production, intracerebral injections and drug treatment
  - Brain histological analysis
  - Immunofluorescence microscopy
  - Mitochondrial membrane potential assay
  - Beta-galactosidase staining of GBM cells
  - Mitochondrial respiration assay using the seahorse XF96 cell mito stress test
  - Beta-galactosidase vs. FSCA and SSCA flow cytometry
  - Beta-galactosidase vs. Ki67 flow cytometry
  - H2B-GFP lentivirus construction
  - H2B-GFP lentivirus production
  - H2B-GFP transduction and selection of L1 and Trp53/Pten(−/−) cells
  - H2B-GFP fluorescence decay studies
  - Western blots
  - Drug synergy
  - STAT3 and BCL-xL shRNAs encoding lentiviral production and transduction
  - Bulk RNA-seq data acquisition and analysis
- QUANTIFICATION AND STATISTICAL ANALYSIS
  - Statistical analysis

## SUPPLEMENTAL INFORMATION

Supplemental information can be found online at https://doi.org/10.1016/j.isci.2024.111311.

Received: June 20, 2024
Revised: September 16, 2024
Accepted: October 30, 2024
Published: November 5, 2024

## REFERENCES

1. Brown, N.F., Ottaviani, D., Tazare, J., Gregson, J., Kitchen, N., Brandner, S., Fersht, N., and Mulholland, P. (2022). Survival Outcomes and Prognostic Factors in Glioblastoma. Cancers *14*, 3161. https://doi.org/10.3390/cancers14133161.
2. Liewer, S., and Huddleston, A. (2018). Alisertib: a review of pharmacokinetics, efficacy and toxicity in patients with hematologic malignancies and solid tumors. Expet Opin. Invest. Drugs *27*, 105–112.
3. Venere, M., Horbinski, C., Crish, J.F., Jin, X., Vasanji, A., Major, J., Burrows, A.C., Chang, C., Prokop, J., Wu, Q., et al. (2015). The mitotic kinesin KIF11 is a driver of invasion, proliferation, and self-renewal in glioblastoma. Sci. Transl. Med. *7*, 304ra143. https://doi.org/10.1126/scitranslmed.aac6762.
4. Gjertsen, B.T., and Schöffski, P. (2015). Discovery and development of the Polo-like kinase inhibitor volasertib in cancer therapy. Leukemia *29*, 11–19.
5. Gampa, G., Kenchappa, R.S., Mohammad, A.S., Parrish, K.E., Kim, M., Crish, J.F., Luu, A., West, R., Hinojosa, A.Q., Sarkaria, J.N., et al. (2020). Enhancing brain retention of a KIF11 inhibitor significantly improves its efficacy in a mouse model of glioblastoma. Sci. Rep. *10*, 6524. https://doi.org/10.1038/s41598-020-63494-7.
6. Oh, J.-H., Power, E.A., Zhang, W., Daniels, D.J., and Elmquist, W.F. (2022). Murine central nervous system and bone marrow distribution of the Aurora A Kinase inhibitor Alisertib: pharmacokinetics and exposure at the sites of efficacy and toxicity. J. Pharmacol. Exp. Therapeut. *383*, 44–55.
7. Dong, J., Park, S.Y., Nguyen, N., Ezhilarasan, R., Martinez-Ledesma, E., Wu, S., Henry, V., Piao, Y., Tiao, N., Brunell, D., et al. (2018). The polo-like kinase 1 inhibitor volasertib synergistically increases radiation efficacy in glioma stem cells. Oncotarget *9*, 10497–10509.
8. Hong, X., O'Donnell, J.P., Salazar, C.R., Van Brocklyn, J.R., Barnett, K.D., Pearl, D.K., deCarvalho, A.C., Ecsedy, J.A., Brown, S.L., Mikkelsen, T., and Lehman, N.L. (2014). The selective Aurora-A kinase inhibitor MLN8237 (alisertib) potently inhibits proliferation of glioblastoma neurosphere tumor stem-like cells and potentiates the effects of temozolomide and ionizing radiation. Cancer Chemother. Pharmacol. *73*, 983–990.
9. Kenchappa, R.S., Dovas, A., Argenziano, M.G., Meyer, C.T., Stopfer, L.E., Banu, M.A., Pereira, B., Griffith, J., Mohammad, A., Talele, S., et al. (2022). Activation of STAT3 through combined SRC and EGFR signaling drives resistance to a mitotic kinesin inhibitor in glioblastoma. Cell Rep. *39*, 110991. https://doi.org/10.1016/j.celrep.2022.110991.
10. Gough, D.J., Corlett, A., Schlessinger, K., Wegrzyn, J., Larner, A.C., and Levy, D.E. (2009). Mitochondrial STAT3 supports Ras-dependent oncogenic transformation. Science *324*, 1713–1716. https://doi.org/10.1126/science.1171721.

11. Wegrzyn, J., Potla, R., Chwae, Y.J., Sepuri, N.B.V., Zhang, Q., Koeck, T., Derecka, M., Szczepanek, K., Szelag, M., Gornicka, A., et al. (2009). Function of mitochondrial Stat3 in cellular respiration. Science *323*, 793–797. https://doi.org/10.1126/science.1164551.

12. Zhang, Q., Raje, V., Yakovlev, V.A., Yacoub, A., Szczepanek, K., Meier, J., Derecka, M., Chen, Q., Hu, Y., Sisler, J., et al. (2013). Mitochondrial localized State3 promotes breast cancer growth via phosphorylation of serine 727. J. Biol. Chem. *288*, 31280–31288. https://doi.org/10.1074/jbc.M113.505057.

13. Hayflick, L. (1965). The limited in vitro lifetime of human diploid cell strains. Exp. Cell Res. *37*, 614–636.

14. Demaria, M., O'Leary, M.N., Chang, J., Shao, L., Liu, S., Alimirah, F., Koenig, K., Le, C., Mitin, N., Deal, A.M., et al. (2017). Cellular senescence promotes adverse effects of chemotherapy and cancer relapse. Cancer Discov. *7*, 165–176.

15. Ruhland, M.K., and Alspach, E. (2021). Senescence and immunoregulation in the tumor microenvironment. Front. Cell Dev. Biol. *9*, 754069. https://doi.org/10.3389/fcell.2021.754069.

16. Demirci, D., Dayanc, B., Mazi, F.A., and Senturk, S. (2021). The Jekyll and Hyde of cellular senescence in cancer. Cells *10*, 208. https://doi.org/10.3390/cells10020208.

17. Fitsiou, E., Soto-Gamez, A., and Demaria, M. (2022). Biological functions of therapy-induced senescence in cancer. Semin. Cancer Biol. *81*, 5–13. https://doi.org/10.1016/j.semcancer.2021.03.021.

18. Pribluda, A., Elyada, E., Wiener, Z., Hamza, H., Goldstein, R.E., Biton, M., Burstain, I., Morgenstern, Y., Brachya, G., Billauer, H., et al. (2013). A senescence-inflammatory switch from cancer-inhibitory to cancer-promoting mechanism. Cancer Cell. *24*, 242–256.

19. Ouchi, R., Oklabe, S., Migita, T., Nakano, I., and Seimiya, H. (2016). Senescence from glioma stem cell differentiation promotes tumor growth. Biochem. Biophys. Res. Commun. *470*, 275–281.

20. Salam, R., Saliou, A., Bielle, F., Bertrand, M., Antoniewski, C., Carpentier, C., Alentorn, A., Capelle, L., Sanson, M., Huillard, E., et al. (2023). Cellular senescence in malignant cells promotes tumor progression in mouse and patient glioblastoma. Nat. Commun. *14*, 441. https://doi.org/10.1038/s41467-023-36124-9.

21. Tejero, R., Huang, Y., Katsyv, I., Kluge, M., Lin, J.Y., Tome-Garcia, J., Daviaud, N., Wang, Y., Zhang, B., Tsankova, N.M., et al. (2019). Gene signatures of quiescent glioblastoma cells reveal mesenchymal shift and interactions with niche microenvironment. EBioMedicine *42*, 252–269.

22. Yie, P., Lopez-Tapia, F., Paladino, D., Li, Y., Chen, C.H., Namanja, A.T., Hilliard, T., Chen, Y., Tius, M.A., Turkson, J., et al. (2016). Hydroxamic Acid and Benzoic Acid–Based STAT3 Inhibitors Suppress Human Glioma and Breast Cancer Phenotypes In Vitro and In Vivo. Cancer Res. *76*, 653–663.

23. Vander Heiden, M.G., Chandel, N.S., Williamson, E.K., Schumacker, P.T., and Thompson, C.B. (1997). Bcl-xL regulates the membrane potential and volume homeostasis of mitochondria. Cell *91*, 627–637.

24. Bruncko, M., Oost, T.K., Belli, B.A., Ding, H., Joseph, M.K., Kunzer, A., Martineau, D., McClellan, W.J., Mitten, M., Ng, S.C., et al. (2007). Studies leading to potent, dual inhibitors of Bcl-2 and Bcl-xL. J. Med. Chem. *50*, 641–662. https://doi.org/10.1021/jm061152t.

25. Wooten, D.J., Meyer, C.T., Lubbock, A.L.R., Quaranta, V., and Lopez, C.F. (2021). MuSyC is a consensus framework that unifies multi-drug synergy metrics for combinatorial drug discovery. Nat. Commun. *12*, 4607.

26. Meyer, C.T., Wooten, D.J., Paudel, B.B., Bauer, J., Hardeman, K.N., Westover, D., Lovly, C.M., Harris, L.A., Tyson, D.R., and Quaranta, V. (2019). Quantifying Drug Combination Synergy along Potency and Efficacy Axes. Cell Syst. *8*, 97–108.e16.

27. Nguyen, T.T.T., Shang, E., Shu, C., Kim, S., Mela, A., Humala, N., Mahajan, A., Yang, H.W., Akman, H.O., Quinzii, C.M., et al. (2021). Aurora kinase A inhibition reverses the Warburg effect and elicits unique metabolic vulnerabilities in glioblastoma. Nat. Commun. *12*, 5203. https://doi.org/10.1038/s41467-021-25501-x.

28. Miller, D.M., Thomas, S.D., Islam, A., Muench, D., and Sedoris, K. (2012). c-Myc and Cancer Metabolism. Clin. Cancer Res. *18*, 5546–5553.

29. Pencik, J., Philippe, C., Schlederer, M., Atas, E., Pecoraro, M., Grund-Gröschke, S., Li, W.J., Tracz, A., Heidegger, I., Lagger, S., et al. (2023). STAT3/LKB1 controls metastatic prostate cancer by regulating mTORC1/CREB pathway. Mol. Cancer *22*, 133.

30. Carro, M.S., Lim, W.K., Alvarez, M.J., Bollo, R.J., Zhao, X., Snyder, E.Y., Sulman, E.P., Anne, S.L., Doetsch, F., Colman, H., et al. (2010). The transcriptional network for mesenchymal transformation of brain tumors. Nature *463*, 318–325.

31. Pantel, K., and Brakenhoff, R.H. (2004). Dissecting the metastatic cascade. Nat. Rev. Cancer *4*, 448–456.

32. Gooding, A.J., and Scheiman, W.P. (2020). Epithelial–Mesenchymal Transition Programs and Cancer Stem Cell Phenotypes: Mediators of Breast Cancer Therapy Resistance. Mol. Cancer Res. *18*, 1257–1270.

33. Colman, H., Zhang, L., Sulman, E.P., McDonald, J.M., Shooshtari, N.L., Rivera, A., Popoff, S., Nutt, C.L., Louis, D.N., Cairncross, J.G., et al. (2010). A multigene predictor of outcome in glioblastoma. Neuro Oncol. *12*, 49–57.

34. Gursel, D.B., Connell-Albert, Y.S., Tuskan, R.G., Anastassiadis, T., Walrath, J.C., Hawes, J.J., Amlin-Van Schaick, J.C., and Reilly, K.M. (2011). Control of proliferation in astrocytoma cells by the receptor tyrosine kinase/PI3K/AKT signaling axis and the use of PI-103 and TCN as potential anti-astrocytoma therapies. Neuro Oncol. *13*, 610–621.

35. Reilly, K.M., Loisel, D.A., Bronson, R.T., McLaughlin, M.E., and Jacks, T. (2000). Nf1;Trp53 mutant mice develop glioblastoma with evidence of strain-specific effects. Nat. Genet. *26*, 109–113.

36. Hambardzumyan, D., Amankulor, N.M., Helmy, K.Y., Becher, O.J., and Holland, E.C. (2009). Modeling Adult Gliomas Using RCAS/t-va Technology. Transl. Oncol. *2*, 89–95.

37. Chen, Z., Giotti, B., Kaluzova, M., Vallcorba, M.P., Rawat, K., Price, G., Herting, C.J., Pinero, G., Cristea, S., Ross, J.L., et al. (2023). A paracrine circuit of IL-1β/IL-1R1 between myeloid and tumor cells drives genotype-dependent glioblastoma progression. J. Clin. Invest. *133*, e163802. https://doi.org/10.1172/JCI163802.

38. Ewald, J.A., Desotelle, J.A., Wilding, G., and Jarrard, D.F. (2010). Therapy-induced senescence in cancer. J. Natl. Cancer Inst. *102*, 1536–1546.

39. Freund, A., Laberge, R.-M., Demaria, M., and Campisi, J. (2012). Lamin B1 loss is a senescence-associated biomarker. Mol. Biol. Cell *23*, 2066–2075.

40. Althubiti, M., Lezina, L., Carrera, S., Jukes-Jones, R., Giblett, S.M., Antonov, A., Barlev, N., Saldanha, G.S., Pritchard, C.A., Cain, K., and Macip, S. (2014). Characterization of novel markers of senescence and their prognostic potential in cancer. Cell Death Dis. *5*, e1528.

41. Lee, H.O., Davidson, J.M., and Duronio, R.J. (2009). Endoreplication: polyploidy with purpose. Genes Dev. *23*, 2461–2477.

42. Shu, Z., Row, S., and Deng, W.-M. (2019). Endoreplication: The Good, the Bad, and the Ugly. Trends Cell Biol. *28*, 465–474.

43. Dirac, A.M.G., and Bernards, R. (2003). Reversal of senescence in mouse fibroblasts through lentiviral suppression of p53. J. Biol. Chem. *278*, 11731–11734.

44. Duy, C., Li, M., Teater, M., Meydan, C., Garrett-Bakelman, F.E., Lee, T.C., Chin, C.R., Durmaz, C., Kawabata, K.C., Dhimolea, E., et al. (2021). Chemotherapy induces senescence-like resilient cells capable of initiating AML recurrence. Cancer Discov. *11*, 1542–1561.

45. Blagden, S.P., Molife, L.R., Seebaran, A., Payne, M., Reid, A.H.M., Protheroe, A.S., Vasist, L.S., Williams, D.D., Bowen, C., Kathman, S.J., et al. (2008). A phase I trial of ispinesib, a kinesin spindle protein inhibitor, with docetaxel in patients with advanced solid tumours. Br. J. Cancer *98*, 894–899.

46. Kaye, S., Aamdal, S., Jones, R., Freyer, G., Pujade-Lauraine, E., de Vries, E.G.E., Barriuso, J., Sandhu, S., Tan, D.S.W., Hartog, V., et al. (2012).

Phase I study of saracatinib (AZD0530) in combination with paclitaxel and/or carboplatin in patients with solid tumours. Br. J. Cancer *106*, 1728–1734.

47. Mosse, Y.P., Fox, E., Teachey, D.T., Reid, J.M., Safgren, S.L., Carol, H., Lock, R.B., Houghton, P.J., Smith, M.A., Hall, D., et al. (2019). A Phase II Study of Alisertib in Children with Recurrent/Refractory Solid Tumors or Leukemia: Children's Oncology Group Phase I and Pilot Consortium (ADVL0921). Clin. Cancer Res. *25*, 3229–3238.
48. Wilson, W.H., O'Connor, O., Czuczman, M.S., LaCasce, A.S., Gerecitano, J.F., Leonard, J.P., Tulpule, A., Dunleavy, K., Xiong, H., Chiu, Y.L., et al. (2010). Safety, pharmacokinetics, pharmacodynamics, and activity of Navitoclax, a targeted high affinity inhibitor of BCL-2, in lymphoid malignancies. Lancet Oncol. *11*, 1149–1159.
49. Catlett-Falcone, R., Landowski, T.H., Oshiro, M.M., Turkson, J., Levitzki, A., Savino, R., Ciliberto, G., Moscinski, L., Fernández-Luna, J.L., Nuñez, G., et al. (1999). Constitutive activation of Stat3 signaling confers resistance to apoptosis in human U266 myeloma cells. Immunity *10*, 105–115.
50. Brabletz, T., Kalluri, R., Nieto, M.A., and Weinberg, R.A. (2018). EMT in cancer. Nat. Rev. Cancer *18*, 128–134.
51. Kim, Y., Varn, F.S., Park, S.-H., Yoon, B.W., Park, H.R., Lee, C., Verhaak, R.G.W., and Paek, S.H. (2021). Perspective of mesenchymal transformation in glioblastoma. Acta Neuropathol. Commun. *9*, 50. https://doi.org/10.1186/s40478-021-01151-4.
52. Cheng, Y.L., Banu, M.A., Zhao, W., Rosenfeld, S.S., Canoll, P., and Sims, P.A. (2024). Multiplexed single-cell lineage tracing of mitotic kinesin inhibitor resistance in glioblastoma. Cell Rep. *43*, 114139. https://doi.org/10.1016/j.celrep.2024.114139.
53. Yuan, J., Crittenden, R.B., and Bender, T.P. (2010). c-Myb promotes the survival of CD4+CD8+ double positive thymocytes through up-regulation of Bcl-xL. J. *Immunol. 184*, 2793–2804.
54. Flor, A.C., Wolfgeher, D., Wu, D., and Kron, S.J. (2017). A signature of enhanced lipid metabolism, lipid peroxidation and aldehyde stress in therapy-induced senescence. Cell Death Dis. *3*, 17075.
55. Saleh, T., Tyutyunyk-Massey, L., Murray, G.F., Alotaibi, M.R., Kawale, A.S., Elsayed, Z., Henderson, S.C., Yakovlev, V., Elmore, L.W., Toor, A., et al. (2019). Tumor cell escape from therapy-induced senescence. Biochem. Pharmacol. *162*, 202–212.
56. Roberson, R.S., Kussick, S.J., Vallieres, E., Chen, S.-Y.J., and Wu, D.Y. (2005). Escape from Therapy-Induced Accelerated Cellular Senescence in p53-Null Lung Cancer Cells and in Human Lung Cancers. Cancer Res. *65*, 2795–2803.
57. Alotaibi, M., Sharma, K., Saleh, T., Povirk, L.F., Hendrickson, E.A., and Gewirtz, D.A. (2016). Radiosensitization by PARP Inhibition in DNA Repair Proficient and Deficient Tumor Cells: Proliferative Recovery in Senescent Cells. Radiat. Res. *185*, 229–245.
58. Holland, A.J., and Cleveland, D.W. (2012). Losing balance: the origin and impact of aneuploidy in cancer. EMBO Rep. *13*, 501–514.
59. Patel, A.P., Tirosh, I., Trombetta, J.J., Shalek, A.K., Gillespie, S.M., Wakimoto, H., Cahill, D.P., Nahed, B.V., Curry, W.T., Martuza, R.L., et al. (2014). Single cell RNA-seq highlights intratumoral heterogeneity in primary glioblastoma. Science *344*, 1396–1401. https://doi.org/10.1126/science.1254257.
60. Neftel, C., Laffy, J., Filbin, M.G., Hara, T., Shore, M.E., Rahme, G.J., Richman, A.R., Silverbush, D., Shaw, M.L., Hebert, C.M., et al. (2019). An Integrative Model of Cellular States, Plasticity, and Genetics for Glioblastoma. Cell *178*, 835–849.e21. https://doi.org/10.1016/j.cell.2019.06.024.
61. Yuan, J., Levitin, H.M., Frattini, V., Bush, E.C., Boyett, D.M., Samanamud, J., Ceccarelli, M., Dovas, A., Zanazzi, G., Canoll, P., et al. (2018). Single-cell transcriptome analysis of lineage diversity in high-grade glioma. Genome Med. *10*, 57. https://doi.org/10.1186/s13073-018-0567-9.
62. Garofano, L., Migliozzi, S., Oh, Y.T., D'Angelo, F., Najac, R.D., Ko, A., Frangaj, B., Caruso, F.P., Yu, K., Yuan, J., et al. (2021). Pathway-based classification of glioblastoma uncovers a mitochondrial subtype with therapeutic vulnerabilities. Nat. Can. (Ott.) *2*, 141–156. https://doi.org/10.1038/s43018-020-00159-4.
63. Wang, L., Lankhorst, L., and Bernards, R. (2022). Exploiting senescence for the treatment of cancer. Nat. Rev. Cancer *22*, 340–355.
64. Loria, R., Vici, P., DiLisa, F.S., Soddu, S., Maugeri-Saccà, M., and Bon, G. (2022). Cross-resistance among sequential cancer therapeutics: an emerging issue. Front. Oncol. *12*, 877380. https://doi.org/10.3389/fonc.2022.877380.
65. Yang, L., Pang, Y., and Moses, H.L. (2010). TGF-β and immune cells: an important regulatory axis in the tumor microenvironment and progression. Trends Immunol. *31*, 220–227.
66. Lei, L., Sonabend, A.M., Guarnieri, P., Soderquist, C., Ludwig, T., Rosenfeld, S., Bruce, J.N., and Canoll, P. (2011). Glioblastoma models reveal the connection between adult glial progenitors and the proneural phenotype. PLoS One *6*, e20041. https://doi.org/10.1371/journal.pone.0020041.
67. Deleyrolle, L.P., Harding, A., Cato, K., Siebzehnrubl, F.A., Rahman, M., Azari, H., Olson, S., Gabrielli, B., Osborne, G., Vescovi, A., and Reynolds, B.A. (2011). Evidence for label-retaining tumour-initiating cells in human glioblastoma. Brain *134*, 1331–1343. https://doi.org/10.1093/brain/awr081.

## STAR★METHODS

### KEY RESOURCES TABLE

| REAGENT or RESOURCE | SOURCE | IDENTIFIER |
|---|---|---|
| **Antibodies** | | |
| Mouse monoclonal ant-Phospho-STAT3 (Tyr705) (M9C6) | Cell Signaling Technology | Cat# 4113 AB_2198588 |
| Rabbit monoclonal ant-Phospho-STAT3 (Ser727) | Cell Signaling Technology | Cat# 9134 AB_331589 |
| Mouse monoclonal anti-STAT3 (124H6) | Cell Signaling Technology | Cat# 9139 AB_331757 |
| Rabbit polyclonal anti-Phospho-Src (Tyr418) | Millipore | Cat# 07-909; RRID: AB_568805 |
| Rabbit polyclonal anti-Src | Cell Signaling Technology | Cat# 2108; RRID: AB_331137 |
| Rabbit monoclonal anti-Phospho-EGF Receptor (Tyr1068) (D7A5) | Cell Signaling Technology | Cat# 3777; RRID: AB_2096270 |
| Rabbit polyclonal anti-EGF Receptor | Cell Signaling Technology | Cat# 2232; RRID: AB_331707 |
| Mouse monoclonal anti-β-Actin (8H10D10) | Cell Signaling Technology | Cat# 3700; RRID: AB_2242334 |
| Mouse monoclonal anti-DDDDK-Tag | MBL International | Cat#M185-3L; RRID: AB_11123930 |
| Rabbit polyclonal Anti-Ki67 | Vector Laboratories | Cat#VP-K451; RRID: AB_2314701 |
| Rabbit monoclonal anti-Ki67 | ThermoFisher Scientific | Cat#MA5-14520; RRID: AB_10979488 |
| Rabbit polyclonal anti-Phospho-AMPK (Thr172, 183) | ThermoFisher Scientific | Cat#44-1150G; RRID: AB_2533585 |
| Rabbit polyclonal anti-AMPK | Cell Signaling Technology | Cat#2532; RRID: AB_330331 |
| Rabbit monoclonal anti-LKB1 | Cell Signaling Technology | Cat#3047: RRID: AB_2198327 |
| Rabbit monoclonal anti-COX IV (3E11) | Cell Signaling Technology | Cat#4850; RRID: AB_2085424 |
| Rabbit monoclonal anti-P21 | Abcam | Cat#AB188224; RRID: AB_2734729 |
| Rabbit polyclonal anti-Phospho-Raptor | Cell Signaling Technology | Cat#2083; RRID: AB_2249475 |
| Rabbit monoclonal anti-Raptor | Cell Signaling Technology | Cat#2280; RRID: AB_561245 |
| Rabbit polyclonal anti-Phospho-TSC2 | Cell Signaling Technology | Cat#5584; RRID: AB_10698883 |
| Rabbit polyclonal anti-TSC-2 | Cell Signaling Technology | Cat#3612; RRID: AB_2207804 |
| Rabbit monoclonal anti-TGF beta1 | Abcam | Cat#AB215715; RRID: AB_2893156 |
| Rabbit monoclonal anti-Phospho-SMAD2 | Cell Signaling Technology | Cat#18338; RRID: AB_2798798 |
| Rabbit monoclonal anti-SMAD2 | Cell Signaling Technology | Cat#5339; RRID: AB_10626777 |
| Rabbit monoclonal anti-Phospho-SMAD3 | Cell Signaling Technology | Cat#9520; RRID: AB_2193207 |
| Rabbit anti-SMAD3 | Cell Signaling Technology | Cat#9513; RRID: AB_2286450 |
| **Bacterial and virus strains** | | |
| PDGF-IRES-Cre retrovirus | Lei et al., 2011[66]; Kenchappa et al.,2020[9] | NA |
| pCW-Cas9 | Addgene | Cat#50661 |
| pLenti Lifeact-EGFP BlastR | Addgene | Cat#84383 |
| H2B-GFP lentivirus | This paper | NA |
| psPAX2 | Addgene | Cat#12260 |
| pMD2.G | Addgene | Cat#12259 |
| **Chemicals, peptides, and recombinant proteins** | | |
| PDGF-AA | Peprotech | Cat# 100-13A |
| hFGF (Human Fibroblast Growth factor) | R&D systems | Cat# 233-FB-025 |
| hEGF (Human Epidermal Growth Factor) | Sigma-Aldrich | Cat# E9644 |
| Fibronectin | Millipore-Sigma | Cat# FC010 |
| Heparin | STEMCELL Technologies | Cat# 07980 |
| N2 supplement | Gibco life technologies | Cat# 17502-048 |
| NeuroPlex supplement | Gemini | Cat# 400-161 |
| Ispinesib | Axon Medchem | Cat# 2446-25 |

(*Continued on next page*)

*Continued*

| REAGENT or RESOURCE | SOURCE | IDENTIFIER |
|---|---|---|
| Alisertib | Selleck Chemicals | Cat#S1133 |
| Volasertib | Selleck Chemicals | Cat#S2235 |
| Metformin | Selleck Chemicals | Cat#S1950 |
| SH5-07 | Selleck Chemicals | Cat# S7923 |
| Saracatinib | Selleck Chemicals | Cat# S1006 |
| Erlotinib | Selleck Chemicals | Cat# S7786 |
| Rhodamine Phalloidin | Cytoskeleton | Cat# PHDR1 |
| VECTASHIELD with DAPI | Vector Laboratories | Cat# U-1500 |
| Formaldehyde, 10% methanol free | CHEM (VWR) | Cat# 87001-890 |
| SUPER signal West Pico PLUS Chemiluminescent substrate | Thermo Fisher Scientific | Cat# 34580 |
| PBS | Thermo Fisher Scientific | Cat# 21-040 |
| PVDF membrane | Biorad | Cat# 1620174 |
| DMSO | Corning | Cat# 25-950-cqc |
| BSA | Thermo Fisher Scientific | Cat# 23209 |
| Non-fat dry milk (Blotting grade blocker) | Biorad | Cat# 170-6404 |
| Accutase | Sigma-Aldrich | Cat# A6964-500 |
| Ethanol | Thermo Fisher Scientific | Cat# 61500-0020 |
| Tween 20 | Sigma-Aldrich | Cat# P1379 |
| TBS | Thermo Fisher Scientific | Cat# 28358 |
| Protease Inhibitor Cocktail, EDTA-free (100X) | Thermo Fisher Scientific | Cat# 87785 |
| Pierce T-1step transfer buffer | Thermo Fisher Scientific | Cat# 84731 |
| Western blot striping buffer | Thermo Fisher Scientific | Cat# 46430 |
| 10X Tris/Glycine/SDS buffer | Biorad | Cat# 1610772 |
| Geltrex | Gibco | Cat# A14132-01 |
| Laminin | Thermo Fisher Scientific | Cat# 3400-010-02 |
| RIPA lysis buffer | Thermo Fisher Scientific | Cat# 89900 |
| B27 supplement | Thermo Fisher Scientific | Cat# A3582801 |
| Laemmli SDS Sample Buffer, reducing, 6X | Thermo Fisher Scientific | Cat# AAJ61337AC |
| Anti-Anti (100x) | Gibco | Cat# 15240-062 |
| D-Luciferin | Perkin Elmer | Cat# 122799 |
| Lipofectamine 3000 transfection agent | Life Technologies | Cat# 11668027 |
| Blasticidine-S-Hydrochloride | Sigma-Aldrich | Cat# SBR00022 |
| Polybrene | Sigma-Aldrich | Cat#TR-1003 |
| Puromycin | InvivoGen | Cat#ant-pr-1 |
| Doxycycline hyclate | Sigma-Aldrich | Cat#D9891 |
| **Critical commercial assays** | | |
| CellTiter-Glo 2.0 assay kit | Promega | Cat# G9242 |
| Pierce™ BCA Protein Assay Kit | Thermo Fisher Scientific | Cat# 23225 |
| RNAqueous™ Total RNA Isolation Kit | Thermo Fisher Scientific | Cat# AM1912 |
| TURBO DNA-free™ Kit | Thermo Fisher Scientific | Cat# AM1907 |
| JC-1 Mitochondrial membrane Potential Assay Kit | Abcam | Cat#AB113850 |
| XF Cell Mito Stress Kit | Allient Technologies | Cat#103708-100 |
| Senescence Beta-Galactosidase Staining Kit | Cell Signaling Technology | Cat#9860 |
| Cellevent™ Senescence Green Detection kit | ThermoFisher Scientific | Cat#C10850 |
| CellEvent™ Senescence Green Flow Cytometry Assay Kit | ThermoFisher Scientific | Cat# C10840 |
| CloneAmp™ HiFi PCR Premix | Takara Bio | Cat#639298 |
| Zymoclean Gel DNA Recovery Kit | Zymo Research | Cat#D4007 |
| T4 DNA Ligase | New England Biolabs | Cat#M0202S |

(*Continued on next page*)

*Continued*

| REAGENT or RESOURCE | SOURCE | IDENTIFIER |
|---|---|---|
| NEB® Stable Competent cells | New England Biolabs | Cat#C3040H |
| Lenti-X™ Concentrator | Takara Bio | Cat#631232 |
| Lenti-X™ p24 Rapid Titer Kit | Takara Bio | Cat#631476 |
| Experimental models: Cell lines | | |
| Trp53/Pten$^{-/-}$ | This paper | NA |
| GBM TS543 | Cheng et al.[52] | NA |
| GBML1 | Deleyrolle et al.[67] | NA |
| GBM612 | Kenchappa et al.[9] | NA |
| MES1861 | Gursel and Reilly et al.[34,35] | NA |
| MES4622 | Gursel and Reilly et al.[34,35] | NA |
| PN20 | Hambardzumyan et al.[36] | NA |
| PN24 | Hambardzumyan et al.[36] | NA |
| Experimental models: Organisms/strains | | |
| Trp53$^{fl/fl}$ mice | Jackson Laboratory | Stock# 008462 |
| Software and algorithms | | |
| Gene Set Enrichment Analysis (GSEA), hallmark analysis (version h.all.v7.0) | Broad Institute | http://software.broadinstitute.org/gse a/index.jsp |
| R Studio | – | https://posit.co/products/open-source/rstudio/ |
| DESeq2 | Open Source | https://github.com/thelovelab/DESeq2 |
| Kallisto | Open Source | https://github.com/pachterlab/kallisto |
| FlowJo | Becton Dickinson | v10.9 |
| FIJI | Open Source | NA |
| SnapGene | SnapGene | v7.1.1 |
| ImageScope | Aperio Technologies | v12.4.6 |
| GraphPad Prism | Graph Pad | v10.3.1 |
| Oligonucleotides | | |
| Primer H2B-V_F: TGGACGAGCTGTAC AAGTAAAGGATCCGGGGTTGGG | This paper | N/A |
| Primer H2B-V_R: GATTTTGCCGGTTC AGGCATGGTGGCGCTAGCCAAT | This paper | N/A |
| Primer H2B-F1_F: GAGAATTGGCTAGCGC CACCATGCCTGAACCGGCAAAATCCG | This paper | N/A |
| Primer H2B-F1_R: GTGGCGACCGGTGGA TCCCCCTTGGAGCTGGTGTACTTGGTG | This paper | N/A |
| Primer H2B-F2_F: CCAAGTACACCAG CTCCAAGGGGGATCCACCGGTC | This paper | N/A |
| Primer H2B-F2_R: CAACCCCAACCCCGGA TCCTTTACTTGTACAGCTCGTCCATGC | This paper | N/A |

## EXPERIMENTAL MODEL AND STUDY PARTICIPANT DETAILS

### Mice

All mouse procedures were performed in compliance with the Mayo Clinic Institutional Animal Care and Use Committee guidelines (protocol numbers A00002923 and A00004179). Homozygous floxed *Trp53* mice in a C57Bl6 background (Stock #008462) were obtained from Jackson Laboratory. Studies were performed on equal numbers of male and female mice between 7 and 12 weeks of age. Animal genotypes were regularly verified via tail snip (TransnetYX, Cordova, TN). Sample sizes were 12 mice per group in the Kaplan Meier survival experiments in Figure 2D and 8 mice per group in the corresponding experiments in Figure 7D. Equal numbers of male and female mice were used in all these experiments, and mice were randomly assigned to each treatment group.

### Cell lines

*Trp53/Pten* deleted glioma cell line isolation from mouse GBM tumor as described by Lei et al., 2011. Murine mesenchymal (MES) glioblastoma cells (MES1861 and MES4622) which lack expression of Nf1 and Trp53 were isolated from mouse GBM tumor and cultured as previously described (Gursel et al., 2011; Reilly et al., 2000), while mouse proneural (PN) glioblastoma cells PN20, PN24 were derived from primary PDGFB-driven glioblastomas generated in Nestin-tva: Cdkn2A knockout mice (Hambardzumyan et al., 2009). Patient derived GBM line L1 was obtained from the laboratory of Dr. Justin D. Lathia (Lerner Research Institute of the Cleveland Clinic Foundation) and GBM line 612 was obtained from the laboratory of Dr. Alfredo Quinones-Hinojosa (Mayo Clinic Florida). The absence of mycoplasma was confirmed regularly by e-Myco TM Mycoplasma PCR Detection Kit (Lilif Diagnostics, Cat# 25235) and cell lines were authenticated using STR analysis (IDEXX BioAnalytics).

## METHOD DETAILS

### Glioma cell line isolation from mouse GBM tumor and culture

The protocol for isolation of tumor cells from *Trp53(−/−)* and *Trp53/Pten(−/−)* murine tumors has been described.[66] Murine mesenchymal (MES) glioblastoma cells (MES1861 and MES4622) which lack expression of Nf1 and Trp53 were maintained in DMEM media with 10% FBS as previously described,[34,35] while mouse proneural (PN) glioblastoma cells PN20, PN24 were derived from primary PDGFB-driven glioblastomas generated in Nestin-tva: Cdkn2A knockout mice[36] and grown in mouse neural stem cell medium (STEMCELL Technologies, 05700 and 05701), supplemented with 20 ng/mL hEGF (Sigma-Aldrich, E9644), 10 ng/mL hFGF (R&D systems, 233-FB-025) and 2 mg/mL heparin (STEMCELL Technologies, 07980). The human L1 primary GBM cell line was cultured and maintained in DMEM+F12 media with 1% N2 supplement (Gibco), 20 ng/mL of hEGF (Sigma-Aldrich) and 20 ng/mL of hFGF (R&D systems). Human GBM612 primary lines were cultured and maintained in DMEM+F12 media with 1% NeuroPlex supplement (Gemini), 20 ng/mL of EGF and 20 ng/mL of FGF. Human GBM TS543 line was cultured and maintained in NeuroCult NS-A medium with proliferation supplement (Stem cell technologies), 20 ng/mL of EGF, 20 ng/mL of FGF and 2ug/mL of heparin. Ispinesib, alisertib or volasertib resistant *Trp53/Pten(−/−)* murine GBM cells were generated by culturing in the presence of 75 nM of ispinesib, 50nM of alisertib or 50nM of volasertib for three weeks, and then maintained at same concentration of these drugs. Ispinesib, alisertib or volasertib resistant human L1, 612 and TS543 GBM cells were generated by culturing in the presence of 25 nM of drug for first week and 50 nM for second and third week, and were maintained in the presence of 50 nM of drug.

### Dose-response curves/cell viability assays

5,000 cells/well were plated in 96-well plates and were allowed to attach for 48 h. Cells were treated with various doses of ispinesib, alisertib, volasertib, saracatinib, SH5-07 or vehicle for 72 h and cell viability was measured using CellTiter-Glo (Promega, cat# G9242).

### Retrovirus production, intracerebral injections and drug treatment

PDGF-IRES-cre retrovirus was generated and injected intracranially according to methods described previously.[9,66] For the pharmacologic studies mice were treated seven days after retroviral injection with vehicle, alisertib (30 mg/kg by oral gavage, 5 days per week), saracatinib (25 mg/kg by oral gavage, 5 days per week), volasertib (10 mg/kg by intraperitoneal injection for every 4 days), or alisertib + saracatinib (alisertib: 30 mg/kg by oral gavage, 5 days per week; saracatinib: 25 mg/kg by oral gavage, 5 days per week) or volasertib + saracatinib (volasertib: 10 mg/kg by intraperitoneal injection for every 4 days; saracatinib: 25 mg/kg by oral gavage, 5 days per week). For simultaneous vs. sequential ispinesib and saracatinib experiments, mice were administered with vehicle, ispinesib (10 mg/kg by intraperitoneal injection every 4 days), ispinesib + saracatinib simultaneously (ispinesib: 10 mg/kg by intraperitoneal injection every 4 days; saracatinib: 25 mg/kg by oral gavage, 5 days per week) or sequentially (alternating cycles of ispinesib 10 mg/kg by intraperitoneal injection for every 4 days for 3 weeks, followed by 1 week of saracatinib 25 mg/kg by oral gavage, 5 days per week). Treatment continued until tumor morbidity.

### Brain histological analysis

Brains from 4% paraformaldehyde-perfused, GBM-bearing mice were paraffin-embedded as described.[9] Immunohistochemistry was performed on 5 mm sections using the Discovery ULTRA automated stainer (Ventana Medical Systems). Antigen retrieval was performed using a Tris/borate/EDTA buffer (Discovery CC1), pH 8.0–8.5, for 60 min at 95°C. Slides were incubated with anti-Ki67 or anti-p21 for 2 h at room temperature. The antibodies were visualized using biotinylated goat anti-rabbit and rabbit anti-rat secondary and counterstained with hematoxylin and eosin (H&E). Images were captured and analyzed using a ScanScope scanner and ImageScope software (Aperio Technologies).

### Immunofluorescence microscopy

Drug naive and resistant GBM cells were grown on glass bottom chamber slides and fixed with ice-cold 4% paraformaldehyde for 20 min at room temperature. After washing with PBS three times, cells were permeabilized with 0.1% Triton X-100 PBS, and then washed three more times with PBS. Cells were incubated with 10% donkey serum in PBST (PBS+ 0.1% Tween 20) for 1h to block non-specific binding of the antibodies, then with Ki67 antibody (MA5-14520, Thermo fisher Scientific) 1:500 in 2% donkey serum in

PBST overnight at 4°C. Following washing, a secondary antibody (donkey anti-rabbit IgG-Alexa 488, Molecular Probes, cat #A21206) diluted 1:500 in PBST was applied to cells and incubated 1 h at room temperature in the dark. Cells were stained for F-actin with Rhodamine Phalloidin (Cytoskeleton Inc, cat #PHDR1, diluted to 100nM final concentration) for 30 min. The slides were then mounted with cover slips using Vectashield (#H-1200; Vector Laboratories). Visualization and imaging of the stained cells were conducted using a confocal microscope (Zeiss LSM 880) with a 10x objective lens. The Alexa Fluor 488 settings were employed to detect the Ki67 signal. Concurrently, images were captured to visualize the Rhodamine phalloidin staining utilizing the Rhodamine settings. Images were acquired from three independent experimental replicates to ensure the reliability and reproducibility of the results.

### Mitochondrial membrane potential assay

To measure the mitochondrial membrane potential in drug naive and ispinesib resistant mouse GBM cells we used JC-1 (tetraethylbenzimidazolylcarbocyanine iodide; Abcam, cat #ab113850). Drug naive and ispinesib resistant cells were cultured on chamber slides. After 72 h, cells were washed once with 1XPBS and treated with 10μm JC-1 solution in dilution buffer for 15 min at 37°C, then washed twice with dilution buffer. In some experiments, ispinesib resistant GBM cells were treated with vehicle or 500nM of erlotinib for 48 h to inhibit EGFR signaling and then added with 10μm of JC-1 solution for 15 min. Live cell imaging was conducted to measure green (FITC) and red (TRITC) fluorescence using a Zeiss confocal microscope (LSM 880) equipped with a 10X objective. The imaging environment was meticulously controlled for temperature, CO2 levels, and humidity to ensure optimal conditions for live cell analysis. In most experiments, a single image was acquired from each of four independent experimental replicates. For experiments involving erlotinib treatment, 3–4 images were captured from each of three independent experimental replicates. The total fluorescence from the entire field of view was quantified using ImageJ software.

### Beta-galactosidase staining of GBM cells

For senescence associated β-galactosidase assay, we used a β-galactosidase staining kit (Cell Signaling Technology, cat#9860). Drug naive and resistant GBM cells were washed once with 1XPBS and fixed in 1X fixative solution for 15 min at room temperature. Cells were then washed two times with 1XPBS and incubated with β-galactosidase staining solution (pH 6.0) at $37^0$C in a dry incubator without the added $CO_2$, and plates were sealed with parafilm to prevent evaporation of the staining medium. After the overnight incubation, cells were washed with 1XPBS and stained images were observed and captured using bright field microscope. In some experiments, ispinesib was withdrawn from ispinesib resistant GBM cells for 24 h, which were then treated with vehicle or 500nM of saracatinib. 72 h later cells were washed once with 1XPBS, fixed with 4% paraformaldehyde for 10 min, washed with PBS containing 1% BSA, and incubated with fluorescent β-galactosidase staining solution (CellEvent Senescence Green Detection Kit, cat# C10850, ThermoFisher Scientific) at $37^0$C in a dry incubator without $CO_2$ for 2 h. Cells were washed with 1XPBS and stained for F-actin and DAPI. Cells were visualized and imaged using confocal microscopy (Zeiss).

### Mitochondrial respiration assay using the seahorse XF96 cell mito stress test

We measured the mitochondrial oxygen consumption rate (OCR) using a Seahorse XFe96 extracellular flux analyzer and a Seahorse XF Cell Mito Stress Test Kit (XF cell mito stress kit, cat#103708-100; XF cell mito stress, cat#103015-100, Agilent Technologies). Drug naive and ispinesib resistant GBM cells were plated in Seahorse XF Cell Culture Miniplates, treated with vehicle or 500nM of erlotinib for 24 h and the Cell Mito Stress assay was performed according to the manufacturer's protocol.

### Beta-galactosidase vs. FSCA and SSCA flow cytometry

Cellular senescence and cellular size and complexity were evaluated in *Trp53*/*Pten*(−/−) murine GBM and L1 human GBM cell lines. Senescence was assessed through flow cytometry employing the CellEvent Senescence Green Flow Cytometry Assay Kit. Drug-resistant cells were generated by exposing *Trp53*/*Pten*(−/−) cells to 75 nM of ispinesib, 50 nM of alisertib, or 50 nM volasertib over a three-week period, followed by maintenance at the same concentrations. Resistant L1 human GBM cells were induced by culturing them in the presence of 25 nM of the respective inhibitors during the first week and 50 nM during the subsequent weeks, with maintenance at 50 nM. For flow cytometric analysis, 500,000 cells were harvested, fixed with 2% PFA, and incubated with a 1:500 dilution of the CellEvent Senescence Green probe for 2 h at 37°C in the dark under an environment devoid of $CO_2$. Data acquisition was carried out using a Cytoflex flow cytometer, measuring β-gal-positive cells. Drug-naïve and non-stained cells were utilized as controls to establish forward and side scatter thresholds and to identify negative and positive β-gal cell populations. Data analysis was performed using FlowJo v10.9 software. All experiments were conducted in triplicate.

### Beta-galactosidase vs. Ki67 flow cytometry

To evaluate cell senescence and proliferation, a flow cytometry-based assay was conducted utilizing *Trp53*/*Pten*(−/−) murine GBM cells under various experimental conditions. The cells were stratified into the following groups: drug-naïve, Ispinesib-resistant, and Ispinesib-resistant treated for 2 days with 500 nM saracatinib. Fluorescent staining of β-gal activity was performed according to the protocol described above. Following β-gal staining, the cells underwent immunofluorescence staining to assess cell proliferation via Ki67 expression using a 1:200 dilution of the primary antibody. Alexa Fluor 594-labeled secondary antibody was utilized to visualize Ki67 positive cells. Sample data were collected using a Cytoflex flow cytometer to quantify β-gal and Ki67 positive cells. Drug-naïve and non-stained cells were utilized as control to set up the flow cytometry analysis and differentiate negative and positive populations

for β-gal and Ki67. Data analysis was performed using FlowJo software version 10.9 to assess the proportions of senescent and proliferative cells within each experimental group. The study was replicated across three independent experiments.

### H2B-GFP lentivirus construction

To generate an inducible H2B-GFP expressing lentiviral construct, a molecular cloning process was employed. Using SnapGene software, the lentiviral vector was designed by incorporating the H2B and GFP (pLenti Lifeact-EGFP BlastR, Addgene #84383) sequences into the plasmid pCW-Cas9 (Addgene #50661). cDNA encoding the histone H2B protein was amplified from SD2 cells (a generous gift of Dr. Roland Friedel, Mount Sinai School of Medicine) following induction with doxycycline. All the PCR reactions were carried out using high-fidelity DNA polymerase (Takara), and specific primers that are detailed in the key resources table. The amplified PCR products were purified via agarose gel extraction. The ligation was conducted using NEBligase, followed by transformation into NEB Stable competent cells. Selection of transformants was performed on ampicillin-containing agar plates, and ampicillin-resistant colonies were expanded for plasmid extraction via miniprep. The integrity of the assembled lentiviral construct was confirmed through enzymatic restriction digestion. Functional validation of the construct was achieved by transfecting HEK cells and inducing expression with doxycycline to ascertain the inducible expression of the H2B-GFP protein.

### H2B-GFP lentivirus production

To generate H2B-GFP lentivirus, HEK-293T cells were cultured under optimal conditions until they reached 80% of confluency for transfection. The cells were subsequently co-transfected with a recombinant lentiviral vector encoding the H2B-GFP protein, along with the psPAX2 and pMD2.G packaging plasmids utilizing Lipofectamine 3000, according to the manufacturer's protocol, in Opti-MEM reduced serum medium. After 6 h of transfection the medium was replaced with complete growth medium to support cell viability and promote viral production. Viral supernatants were harvested at two sequential time points: 24- and 48-h post-transfection. These supernatants were combined to maximize viral yield. Following collection, the lentiviral particles were concentrated using the Lenti-X concentrator system as per the manufacturer's guidelines. The concentration of viral particles was quantified using a p24 ELISA assay.

### H2B-GFP transduction and selection of L1 and Trp53/Pten(−/−) cells

To investigate the proliferative behavior of GBM cells, we employed two distinct cell lines: L1 (*human GBM*) and *Trp53/Pten*(−/−) (*murine GBM*). These lines were genetically engineered to express H2B-GFP. The transduction process was carried out using a lentiviral vector encoding the H2B-GFP construct, described above. Cells were incubated with the viral particles in complete medium containing 4 μg/mL polybrene at an MOI of 50 for 72 h. After transduction, cells were selected for stable integration of the H2B-GFP construct with 1.5 μg/mL puromycin for two weeks and selection by FACS with the Aria cytometer. The expression and functionality of H2B-GFP were validated through fluorescence microscopy after the induction of with 2 μg/mL doxycycline in complete medium for 48 h.

### H2B-GFP fluorescence decay studies

H2B-GFP fluorescence decay was assessed using lentiviral transduced L1 human GBM cells and *Trp53/Pten*(−/−) murine GBM cells, both expressing inducible H2B-GFP protein. To generate resistant cell lines, cells were subjected to ispinesib, alisertib, or volasertib treatment for three weeks, as described above. Induction of H2B-GFP expression was achieved by adding 2 μg/mL doxycycline to the culture medium for 48 h. Following induction, the medium was replaced with fresh medium, and the decay of GFP fluorescence intensity was monitored over a 24-day period at various time points using a Zeiss LSM 880 confocal microscope. Quantification of fluorescence in the confocal images was conducted using ImageJ software. Data analysis was performed with GraphPad software.

### Western blots

Cells were scraped and incubated in lysis buffer (50 mM Tris HCl at pH 7.40, 150 mM NaCl, 1 mM EDTA, 1.0% Nonidet P-40, and a mixture of protease and phosphatase inhibitors), on ice from 30 min. Debris was removed by centrifugation for 10 min at high speed at 4°C, and cleared lysates were run on SDS/PAGE and transferred to polyvinylidene difluoride membranes. Membranes were blocked in 5% non-fat dry milk in TBS +0.1% Tween 20 for 1 h at room temperature, incubated with primary antibody in blocking solution for overnight at 4°C, followed by secondary antibody for 1 h at room temperature, and developed using an enhanced chemiluminescence solution.

### Drug synergy

Synergy was calculated using the MuSyC algorithm as previously described.[25,26] MuSyC quantifies two types of drug synergy, synergistic potency and synergistic efficacy, both relating to geometric transformations of the dose response surface, which are analogous to the transformations in the 1D Hill equation for potency (horizontal shift in the $EC_{50}$) and efficacy (vertical shift in $E_{max}$). Synergy was calculated by fitting a dose-response surface relating the drug's effect to the concentrations of drug 1 and drug 2. To help the growth-rate-based fits converge, the bounds for $E_0$ (effect with no drug) and $E_1$, $E_2$, $E_3$ (maximal effects of drug 1, 2, and the combination) were set to [0.005, 0.002] and [0.01, −0.01], respectively.

### STAT3 and BCL-xL shRNAs encoding lentiviral production and transduction

Knockdown of STAT3 and BCL-xL in GBM cells was achieved via lentiviral infection with shRNA-encoding constructs. The lentiviral plasmid vector pLKO.1-puro based shRNA clones and control shRNA vector were purchased from Sigma-Aldrich (St Louis, MO, USA). The following constructs were used for murine GBM cells in these studies: Non Targeting control (SHC002); STAT3 sh-RNA [TRCN0000071454 (STAT3-shRNA-1), TRCN0000071456 (STAT3-shRNA-2), BCL_XL shRNA [TRCN0000004682], BCL_XL shRNA [TRCN0000010905]. Each of the pLK0.1 targeting constructs were co-transfected with psPAX2 and pMD plasmids into HEK-293T cells via Lipofectamine 3000 transfection agent (Life Technologies, catalog # 11668027) in serum-free medium. After 8 h of transfection, the viral particle-containing medium was removed and replaced with fresh complete medium. Transfected cells were then grown in DMEM media containing 10% FBS for 48 h at 37°C, 5% CO2. Media containing virus was harvested and centrifuged for 10 min in a clinical specimen centrifuge and then filtered through a 0.45 μm filter. Lentiviral particles were concentrated using LentiX-Concentrator reagent (Takara Bio USA) and the viral titer was determined using a p24 ELISA kit (Clontech). Mouse glioma cells were infected by incubating with virus containing media (at 10 MOI of virus and 4 μg/mL of polybrene (Sigma-Aldrich)) overnight. Cells were selected for positive shRNA infection using puromycin (0.5ug/mL) for seven days and maintained in 0.1ug/mL puromycin containing media, and then effect of STAT3 and BCL_XL knockdown on cell viability was measured.

### Bulk RNA-seq data acquisition and analysis

RNA sequencing was performed at the Columbia Sulzberger Genome Center. Total RNA from three independent biological replicates (naive and ispinesib resistant cells) was isolated using the RNAqueous phenol-free total RNA isolation kit (Ambion, Life Technologies, Grand Island, NY) and DNA contamination in isolated RNA was removed by DNase treatment using TURBO DNA-free kit (Ambion, Life Technologies, CA). All samples had an RNA Integrity Number greater than 7.6, as assessed using Agilent Bioanalyzer. Libraries were prepared using the Illumina TruSeq RNA Library Prep Kit v2 and 20 million paired-end, 75 bp reads were acquired on an Element Aviti sequencer at Columbia Genome Center. Reads were pseudoaligned to a kallisto mouse transcriptome index (GRCm38.p6) using kallisto (0.44.0), and differential gene expression analysis was determined using DESeq2. Gene Set Enrichment Analysis (GSEA) was performed on the desktop version of GSEA (v4.1.0), using Hallmarks (Liberzon et al., 2015) and the Verhaak_Glioblastoma._mesenchymal gene sets from the Molecular Signatures Database (MSigDB).

## QUANTIFICATION AND STATISTICAL ANALYSIS

### Statistical analysis

Data from repeated measurements are depicted as the mean ±1 standard deviation. For quantification of Western blot intensities, at least three biological replicates were performed, and statistical significance was determined using pairwise, two tailed t tests with significance defined as $p < 0.05$. For the Kaplan Meier survival curves in Figure 2D, sample size was 12 mice per group. The significance of differences in median survival was determined using pairwise log-rank tests, with significance set at $p < 0.05$. For the corresponding Kaplan Meier survival curves in Figure 7D, sample size was 8 mice per group, with statistical significance determined by log-rank test as above. For the cell viability measurements in Figure 2F, measurements were performed on 96 well plates for each condition, and significance was determined with two tailed t tests as above. Fluorescence ratio measurements in Figures 3A, 3B, and 3D were performed on at least 4 biological replicates, and significance determined by two tailed t tests. The growth rates in Figures 6C–6H were determined by linear least squares fitting after logarithmic transformation of the data, and each measurement represents the mean ±1 SD of 8 biological replicates. Statistical significance of differences in slopes of the resulting curves, corresponding to growth rates, was determined by sequential two tailed t test with significance set at $p < 0.05$.